ZAMM · Z. Angew. Math. Mech. 1–27 (2015) / **DOI** 10.1002/zamm.201400087

Implicit co-simulation methods: Stability and convergence analysis for solver coupling approaches with algebraic constraints

Bernhard Schweizer*, **Pu Li, and Daixing Lu**

Department of Mechanical Engineering, Institute of Applied Dynamics, Technical University Darmstadt, Germany

Received 23 April 2014, revised 28 May 2015, accepted 15 June 2015
Published online 3 November 2015

Key words Co-simulation, solver coupling, subcycling, implicit, algebraic constraints, stability, convergence.
MSC (2010) 04A25

The analysis of the numerical stability of co-simulation methods with algebraic constraints is subject of this manuscript. Three different implicit coupling schemes are investigated. The first method is based on the well-known Baumgarte stabilization technique. Basis of the second coupling method is a weighted multiplier approach. Within the third method, a classical projection technique is applied. The three methods are discussed for different approximation orders. Concerning the decomposition of the overall system into subsystems, we consider all three possible approaches, i.e. force/force-, force/displacement- and displacement/displacement-decomposition. The stability analysis of co-simulation methods with algebraic constraints is inherently related to the definition of a test model. Bearing in mind the stability definition for numerical time integration schemes, i.e. Dahlquist's stability theory based on the linear single-mass oscillator, a linear two-mass oscillator is used here for analyzing the stability of co-simulation methods. The two-mass co-simulation test model may be regarded as two Dahlquist equations, coupled by an algebraic constraint equation. By discretizing the co-simulation test model with a linear co-simulation approach, a linear system of recurrence equations is obtained. The stability of the recurrence system, which reflects the stability of the underlying coupling method, can simply be determined by an eigenvalue analysis.

1 Introduction

Starting with the fundamental work in Ref. [17], diverse co-simulation methods have been developed in the following in order to couple two (or several) solvers in time domain. The basic idea behind a co-simulation approach consists in a decomposition of the overall system into two (or several) subsystems. Regarding the decomposition, three different topological approaches can be distinguished for mechanical systems, namely the force/force-, the force/displacement- and the displacement/displacement-decomposition approach [4, 16, 36]. Equivalent decomposition techniques exist for non-mechanical systems. Concerning the coupling of the subsystems, two different approaches exist. Firstly, the subsystems can be coupled by algebraic constraint equations (i.e. by rigid joints). In this case, reaction forces/torques are used to describe the interaction between the subsystems [20, 25, 34, 35, 37, 40, 41]. Secondly, the subsystems may be coupled by constitutive laws (i.e. by physical force/torque laws). Then, applied forces/torques are used to define the subsystem interaction [8, 16, 18, 23, 24, 38, 39, 44]. Solver or simulator coupling has been used in a large number of applications. Co-simulation has advantageously been applied in the field of vehicle dynamics, see for instance Refs. [12, 13, 27, 30] or in context with fluid/structure interaction problems [7, 14, 28, 32]. For the coupled simulation of multibody and finite-element systems, co-simulation has also been successfully applied, see Refs. [1, 2, 5]. Coupled interaction problems including mutibody and particle models are examined in Refs. [15, 26, 42]. In Refs. [29, 33], multibody and hydraulic systems are coupled by means of a co-simulation approach. Co-simulations are frequently accomplished with equidistant communication-time grids. Coupling approaches with variable macro-step sizes are for instance discussed in Refs. [6, 43].

The numerical stability of co-simulation methods has been investigated by different authors. For the stability analysis, usually simple test models are used. In Ref. [25], a double pendulum is applied as test model in connection with constraint coupling. A two-mass oscillator with two degrees of freedom is employed in Refs. [4, 16, 19] for analyzing solver coupling in context with applied force/torque coupling. A mere mathematical test-model with 4 parameters is used in Ref. [43] for the analysis of a special co-simulation approach in combination with BDF-integrators. Different simple test models have also been considered in connection with explicit subcycling methods in finite element applications, see Refs. [9–11] (note that subcycling methods may be regarded as explicit co-simulation approaches). In this manuscript, a stability analysis

* Corresponding author E-mail: schweizer@sds.tu-darmstadt.de, Phone: +49-6151-16-3461, Fax: +49-6151-16-3668

is presented for three implicit co-simulation methods based on a general 5 parameter test model. In accordance with the stability analysis for time integration schemes, we ride on the assumption that the macro-step size is constant. Since the test model is linear, the subsystem integration can be carried out analytically. Thus, stabilizing or destabilizing effects due to the subsystem integration are not present in our analysis and a multirate factor has not to be taken into account [17, 19, 25]. Our results only reflect numerical instabilities introduced by the co-simulation, i.e. by the weak coupling approach. Furthermore, we assume that the subsystems are integrated in parallel (Jacobi type). In practical applications, where the subsystems are integrated numerically, the subsystem solver will influence the stability of the co-simulation. A detailed stability analysis, which also takes into account the subsystem solver, is complicated and depends on the integration scheme used for solving the subsystems. It should also be stressed that the presented stability analysis is defined – according to Dahlquist's stability theory for time integration schemes – on the basis of a linear test model. Predicting the stability of nonlinear co-simulation models by means of stability plots generated with a linear test model, might in general be difficult. As in the case of time integration schemes, stability plots may, however, be very useful in order to get a general impression of the numerical stability of coupling approaches and in order to compare different co-simulation methods with respect to their numerical stability behavior.

This manuscript can be regarded as a follow-up work with respect to Ref. [34]. In the previous paper, two methods for solver coupling with algebraic constraints were presented, namely a coupling approach based on Baumgarte stabilization and a coupling method on the basis of a weighted multiplier approach. Here, we also consider a third method, which makes use of a projection technique. In Ref. [34], stability of the Baumgarte and weighted multiplier method has just been investigated by straightforward numerical time integrations. Stability plots have been generated only as a function of two parameters, namely stiffness and damping coefficients of the test system. In the current manuscript, we present an analytical stability analysis based on the solution of an eigenvalue problem for a general 5 parameter co-simulation test model. In Ref. [34], the coupling methods based on Baumgarte stabilization and on the weighted multiplier approach are investigated only for the case that the subsystems are connected by a force/force-coupling approach. Here, we consider three coupling approaches (Baumgarte, weighted multiplier and projection approach) and we discuss – in contrast to Ref. [34] – all three decomposition techniques (force/force-, force/displacement- and displacement/displacement-decomposition). Stability plots are presented with respect to the five independent (dimensionless) parameters of the co-simulation test model.

For analyzing the stability of co-simulation approaches, it is useful to apply and extend the definition of the numerical stability of time integration methods [21, 22], which is based on Dahlquist's test equation

$$\dot{y}(t) = \lambda \cdot y(t). \tag{1}$$

In the above equation, $y(t)$ represents a scalar function of time and $\lambda \in \mathbb{C}$ an arbitrary complex constant. $\dot{y} = dy/dt$ denotes the derivative of y with respect to time t. There exists a simple mechanical interpretation of Dahlquist's test equation. From the mechanical point of view, Eq. (1) can be regarded as the complex representation of the equations of motion of the linear single-mass oscillator. This can easily be shown by considering the homogenous linear mass-spring-damper oscillator (mass m, spring constant c and damping coefficient d), whose equations of motion are given by

$$\begin{pmatrix} \dot{x} \\ \dot{v} \end{pmatrix} = \begin{pmatrix} 0 & 1 \\ -\frac{c}{m} & -\frac{d}{m} \end{pmatrix} \begin{pmatrix} x \\ v \end{pmatrix}. \tag{2}$$

As usual, x and v term the position and the velocity of the oscillator. The complex eigenvalues of Eq. (2) are $\lambda_{1,2} = \lambda_r \pm i\lambda_i = -\frac{d}{2m} \pm i \cdot \frac{\sqrt{4m \cdot c - d^2}}{2m}$. The corresponding eigenvectors are $(1 \ \lambda_1)^T$ and $(1 \ \lambda_2)^T$. With the help of the modal matrix $\boldsymbol{Q} = \begin{pmatrix} 1 & 1 \\ \lambda_1 & \lambda_2 \end{pmatrix}$ and with the modal coordinates $\begin{pmatrix} y_1 \\ y_2 \end{pmatrix} = \boldsymbol{Q}^{-1} \begin{pmatrix} x \\ v \end{pmatrix}$, Eq. (2) can be transformed into the two decoupled equations

$$\begin{pmatrix} \dot{y}_1 \\ \dot{y}_2 \end{pmatrix} = \begin{pmatrix} \lambda_1 & 0 \\ 0 & \lambda_2 \end{pmatrix} \begin{pmatrix} y_1 \\ y_2 \end{pmatrix}. \tag{3}$$

Discretizing Dahlquist's test equation with a linear time integration scheme (e.g. with a Runge-Kutta or BDF method) and assuming a constant integration-step size h, one obtains a linear recurrence equation. The solution of this recurrence equation yields the discretized values y_n $(n = 0, 1, 2, \ldots)$, which represent an approximation of the analytical solution $y(t_n)$ at the time points t_n. Assuming that $m, c, d > 0$, the single-mass oscillator is a stable mechanical system, the solution of which is described by a damped oscillation. If the discretized Dahlquist equation yields a sequence of exponentially decaying values y_n for $m, c, d > 0$, the underlying time integration scheme is called numerically stable. As well-known, the stability behavior of time integration methods depends on the two independent parameters $h\lambda_r$ and $h\lambda_i$. In literature, stable regions of the integration scheme are commonly illustrated in 2D stability plots as a function of $h\lambda_r$ and $h\lambda_i$.

For defining and investigating the numerical stability of co-simulation methods with algebraic constraints, we use the linear two-mass oscillator depicted in Fig. 1. This oscillator consists of two single-mass oscillators (masses m_1, m_2, spring constants c_1, c_2, damping coefficients d_1, d_2), which are connected by a rigid link. Hence, the two-mass oscillator may be interpreted as two Dahlquist equations, which are coupled by the algebraic constraint equation $x_2 - x_1 = 0$.

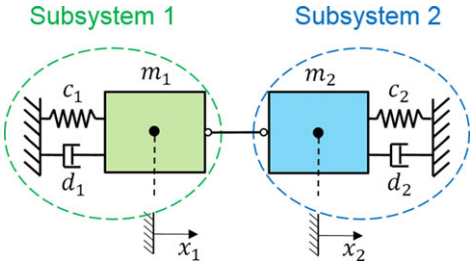

Fig. 1 Linear two-mass oscillator: test model for analyzing the numerical stability of co-simulation methods with algebraic constraints.

The equations of motion for the coupled oscillator are given by the index-3 DAE system

$$\begin{aligned} \dot{x}_1 &= v_1, & \dot{v}_1 &= -\frac{c_1}{m_1}x_1 - \frac{d_1}{m_1}v_1 + \frac{1}{m_1}\lambda_c, \\ \dot{x}_2 &= v_2, & \dot{v}_2 &= -\frac{c_2}{m_2}x_2 - \frac{d_2}{m_2}v_2 - \frac{1}{m_2}\lambda_c, \\ 0 &= x_2 - x_1, \end{aligned} \tag{4}$$

where x_1, x_2 and v_1, v_2 denote position and velocity of the two masses and λ_c the Lagrange multiplier.

For the following stability analysis, it is convenient to define the 5 subsequent parameters:

$$\bar{c}_1 = \frac{c_1 \cdot H^2}{m_1}, \quad \bar{d}_1 = \frac{d_1 \cdot H}{m_1}, \quad \alpha_{m21} = \frac{m_2}{m_1}, \quad \alpha_{c21} = \frac{c_2}{c_1}, \quad \alpha_{d21} = \frac{d_2}{d_1}. \tag{5}$$

Introducing furthermore the dimensionless time $\bar{t} = \frac{t}{H}$, where H terms the macro-step size of the co-simulation approach, see Sect. 2, Eq. (4) can be rewritten as

$$\begin{aligned} \bar{x}_1' &= \bar{v}_1, & \bar{v}_1' &= -\bar{c}_1 \cdot \bar{x}_1 - \bar{d}_1 \cdot \bar{v}_1 + \bar{\lambda}_c, \\ \bar{x}_2' &= \bar{v}_2, & \bar{v}_2' &= -\frac{\alpha_{c21}}{\alpha_{m21}} \cdot \bar{c}_1 \cdot \bar{x}_2 - \frac{\alpha_{d21}}{\alpha_{m21}} \cdot \bar{d}_1 \cdot \bar{v}_2 - \frac{1}{\alpha_{m21}} \cdot \bar{\lambda}_c, \\ 0 &= \bar{x}_2 - \bar{x}_1. \end{aligned} \tag{6}$$

Note that $\bar{x}_1 = \frac{x_1}{l}, \bar{x}_2 = \frac{x_2}{l}$ are dimensionless position coordinates (l is a properly chosen characteristic length). $\bar{v}_1 = \frac{H \cdot v_1}{l}$ and $\bar{v}_2 = \frac{H \cdot v_2}{l}$ represent dimensionless velocities and $\bar{\lambda}_c = \frac{\lambda_c \cdot H^2}{m_1 \cdot l}$ the dimensionless Lagrange multiplier. $(\cdot)' = \frac{d(\cdot)}{d\bar{t}}$ denotes the derivative with respect to the dimensionless time $\bar{t}$. Assuming that $m_1, m_2, c_1, c_2, d_1, d_2 > 0$, the two-mass oscillator is a stable mechanical system. Discretizing Eq. (6) with a linear co-simulation method results in a homogenous linear system of recurrence equations, see Sect. 2. By calculating the spectral radius, the stability of the recurrence system can be determined. If the spectral radius is smaller than 1, the recurrence system – and therefore the underlying co-simulation method – is called numerically stable. The spectral radius is a function of the 5 independent parameters defined in Eq. (5). Fixing three parameters, the spectral radius can be plotted in 2D stability diagrams as a function of the remaining 2 parameters.

This manuscript is structured as follows: In Sect. 2, the governing systems of recurrence equations are derived for three implicit co-simulation methods. Results of the stability and convergence analysis are discussed in Sect. 3. A nonlinear example is presented in Sect. 4. The paper is summarized in Sect. 5. For the reason of a clear representation, the 2D stability plots for the three co-simulation methods are arranged in the Appendices A-F. Convergence plots are collected in Appendix G (see Wiley online library).

2 Test model and systems of recurrence equations for three implicit co-simulation methods

Making use of a co-simulation approach, the overall system is decomposed into two (or several) subsystems. Concerning the decomposition, three different techniques can be applied: the force/force-, the force/displacement- and the

displacement/displacement-decomposition approach. For the numerical simulation of the decomposed system, the connection between the subsystems has to be specified and appropriate coupling variables have to be introduced. Moreover, a macro-time grid – i.e. macro-time points $T_0, T_1, \ldots, T_N$ – has to be defined. In this manuscript, we assume that the macro-step size $H = T_{N+1} - T_N$ is constant. Within a co-simulation approach, the subsystems are coupled in a weak sense [1, 8, 17, 18], i.e. the two subsystems are integrated independently between the macro-time points. Only at the macro-time points information is exchanged between the subsystems. As a consequence, the coupling variables have to be approximated during the subsystem integration from T_N to T_{N+1} using extrapolation/interpolation techniques. In this work, Lagrange polynomials are used for approximating the coupling variables. Furthermore, we assume that the subsystems are integrated in parallel (Jacobi type). The extension to sequential integration schemes (Gauss-Seidel type) is straightforward and is not discussed here. In the following subsections, three implicit co-simulation methods – a method based on Baumgarte stabilization, a weighted multiplier approach and a projection method – are examined considering all three decomposition approaches (force/force-, force/displacement- and displacement/displacement-decomposition).

2.1 Force/Force-coupling

2.1.1 Implicit co-simulation method based on baumgarte stabilization

Applying a force/force-decomposition technique to split the co-simulation test model into two subsystems, one obtains two force-driven single-mass oscillators, see Fig. 2. Both masses are driven by the coupling force λ_c.

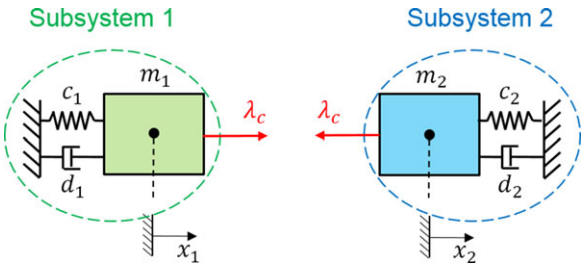

Fig. 2 Co-simulation test model: force/force-decomposition approach.

Using the dimensionless variables $\bar{x}_1, \bar{x}_2, \bar{v}_1, \bar{v}_2$ and $\bar{\lambda}_c$ as well as the parameters from Eq. (5), the decomposed system is described by the following DAE system

Subsystem 1:

$$\bar{x}_1' = \bar{v}_1, \qquad \bar{v}_1' = -\bar{c}_1 \cdot \bar{x}_1 - \bar{d}_1 \cdot \bar{v}_1 + \bar{\lambda}_c, \tag{7a}$$

Subsystem 2:

$$\bar{x}_2' = \bar{v}_2, \qquad \bar{v}_2' = -\frac{\alpha_{c21}}{\alpha_{m21}} \cdot \bar{c}_1 \cdot \bar{x}_2 - \frac{\alpha_{d21}}{\alpha_{m21}} \cdot \bar{d}_1 \cdot \bar{v}_2 - \frac{1}{\alpha_{m21}} \cdot \bar{\lambda}_c, \tag{7b}$$

Coupling condition:

$$\bar{g}_{c\lambda}^{B} := (\bar{x}_2 - \bar{x}_1) + \bar{\beta} \cdot (\bar{v}_2 - \bar{v}_1) + \bar{\gamma} \cdot (\bar{v}_2' - \bar{v}_1') = 0. \tag{7c}$$

Note that the constraint equation $\bar{x}_2 - \bar{x}_1 = 0$ in Eq. (6) has been modified by using the well-known Baumgarte stabilization technique [3]. $\bar{\beta} > 0$ and $\bar{\gamma} > 0$ are real-valued parameters, which have to be specified by the user. It should be mentioned that $\bar{\beta} = \beta/H$ and $\bar{\gamma} = \gamma/H^2$ denote dimensionless Baumgarte parameters.

In the following, the general macro-step from $\bar{T}_N$ to $\bar{T}_{N+1}$ is considered and the system of recurrence equations for the discretized test-model is derived. It should be mentioned that $\bar{T}_N = T_N/H$ denotes the dimensionless macro-time point. In order to integrate the subsystems from $\bar{T}_N$ to $\bar{T}_{N+1}$, it is necessary to approximate the coupling variable $\bar{\lambda}_c(\bar{t})$ in the time interval $[\bar{T}_N, \bar{T}_{N+1}]$. Here, the approximation is accomplished with Lagrange polynomials of degree k. For the definition of the Lagrange polynomials, $k+1$ sampling points have to be specified. For instance, using the $k+1$ sampling points $(\bar{T}_N, \bar{\lambda}_{c,N}), (\bar{T}_{N-1}, \bar{\lambda}_{c,N-1}), \ldots, (\bar{T}_{N-k}, \bar{\lambda}_{c,N-k})$, we get a polynomial of degree k, which we abbreviate by $P_{\bar{\lambda}_c}[(\bar{T}_N, \bar{\lambda}_{c,N}), (\bar{T}_{N-1}, \bar{\lambda}_{c,N-1}), \ldots, (\bar{T}_{N-k}, \bar{\lambda}_{c,N-k}); \bar{t}]$.

At the beginning of the macro-time step, the state variables and the coupling variable are assumed to be known

$$\bar{x}_1(\bar{T}_N) = \bar{x}_{1,N}, \qquad \bar{v}_1(\bar{T}_N) = \bar{v}_{1,N},$$
$$\bar{x}_2(\bar{T}_N) = \bar{x}_{2,N}, \qquad \bar{v}_2(\bar{T}_N) = \bar{v}_{2,N}, \tag{8a}$$
$$\bar{\lambda}_c(\bar{T}_N) = \bar{\lambda}_{c,N}. \tag{8b}$$

For higher order approximation ($k > 0$), we further assume that the coupling variables at the previous k macro-time points $\bar{T}_{N-1}, \ldots, \bar{T}_{N-k}$ are known.

The implicit co-simulation approach considered in this subsection is a predictor/corrector approach, which can be subdivided into 3 steps. In the following representation, predicted variables are indicated with an upper index p (e.g. $\bar{x}^p_{1,N+1}$). Variables without upper index are assumed to be corrected variables (e.g. $\bar{x}_{1,N+1}$). For the subsequent analysis, it is useful to define the vectors $\boldsymbol{z}_N = (\bar{x}_{1,N}, \bar{v}_{1,N}, \bar{x}_{2,N}, \bar{v}_{2,N})^T$, $\boldsymbol{z}_{N-1} = (\bar{x}_{1,N-1}, \bar{v}_{1,N-1}, \bar{x}_{2,N-1}, \bar{v}_{2,N-1})^T, \ldots, \boldsymbol{z}_{N-k} = (\bar{x}_{1,N-k}, \bar{v}_{1,N-k}, \bar{x}_{2,N-k}, \bar{v}_{2,N-k})^T$, which collect the state variables of both subsystems at the macro-time points $\bar{T}_N$, $\bar{T}_{N-1}, \ldots, \bar{T}_{N-k}$.

Step 1: Predictor Step

- By analytically integrating subsystem 1 and subsystem 2 from $\bar{T}_N$ to $\bar{T}_{N+1}$ with the initial conditions (8a) and with the predictor (extrapolation) polynomial

$$\bar{\lambda}^p_c(\bar{t}) = P^p_{\bar{\lambda}_c}\left[\left(\bar{T}_N, \bar{\lambda}_{c,N}\right), \left(\bar{T}_{N-1}, \bar{\lambda}_{c,N-1}\right), \ldots, \left(\bar{T}_{N-k}, \bar{\lambda}_{c,N-k}\right); \bar{t}\right], \tag{9}$$

  one obtains the predicted state variables

$$\bar{x}^p_{1,N+1}, \quad \bar{v}^p_{1,N+1} \quad \text{and} \quad \bar{x}^p_{2,N+1}, \quad \bar{v}^p_{2,N+1} \tag{10}$$

  at the macro-time point $\bar{T}_{N+1}$. It should be stressed that the predicted variables are depending on $\bar{\lambda}_{c,N}$, $\bar{\lambda}_{c,N-1}$, …, $\bar{\lambda}_{c,N-k}$ and $\boldsymbol{z}_N$.

Step 2: Calculation of Corrected Coupling Force

- An analytical integration of subsystem 1 and subsystem 2 from $\bar{T}_N$ to $\bar{T}_{N+1}$ with the initial conditions (8a) and with the interpolation polynomial

$$\bar{\lambda}^*_c(\bar{t}) = P^*_{\bar{\lambda}_c}\left[\left(\bar{T}_{N+1}, \bar{\lambda}^*_{c,N+1}\right), \left(\bar{T}_N, \bar{\lambda}_{c,N}\right), \ldots, \left(\bar{T}_{N-k+1}, \bar{\lambda}_{c,N-k+1}\right); \bar{t}\right] \tag{11}$$

  yields the state variables

$$\bar{x}^*_{1,N+1}, \quad \bar{v}^*_{1,N+1} \quad \text{and} \quad \bar{x}^*_{2,N+1}, \quad \bar{v}^*_{2,N+1} \tag{12}$$

  at the macro-time point $\bar{T}_{N+1}$, which depend on $\bar{\lambda}^*_{c,N+1}$, $\bar{\lambda}_{c,N}, \ldots, \bar{\lambda}_{c,N-k+1}, \boldsymbol{z}_N$. Please note that $\bar{\lambda}^*_{c,N+1}$ represents an arbitrary coupling force at the macro-time point $\bar{T}_{N+1}$.
- By differentiating the state variables of Eq. (12) and the corresponding accelerations with respect to $\bar{\lambda}^*_{c,N+1}$, we get the partial derivatives

$$\begin{aligned} \frac{\partial \bar{x}^*_{1,N+1}}{\partial \bar{\lambda}^*_{c,N+1}} &= const., \quad \frac{\partial \bar{v}^*_{1,N+1}}{\partial \bar{\lambda}^*_{c,N+1}} = const., \quad \frac{\partial \bar{v}'^*_{1,N+1}}{\partial \bar{\lambda}^*_{c,N+1}} = const., \\ \frac{\partial \bar{x}^*_{2,N+1}}{\partial \bar{\lambda}^*_{c,N+1}} &= const., \quad \frac{\partial \bar{v}^*_{2,N+1}}{\partial \bar{\lambda}^*_{c,N+1}} = const., \quad \frac{\partial \bar{v}'^*_{2,N+1}}{\partial \bar{\lambda}^*_{c,N+1}} = const.. \end{aligned} \tag{13}$$

  It should be stressed that the partial derivatives are constant, because the state variables of Eq. (12) and the corresponding accelerations only depend linearly on $\bar{\lambda}^*_{c,N+1}$.
- With the predicted variables and with the partial derivatives, a corrected coupling force $\bar{\lambda}_{c,N+1}$ can be computed, which fulfills the coupling condition (7c) at the macro-time point $\bar{T}_{N+1}$. Considering the fixed time point $\bar{T}_{N+1}$, $\bar{g}^B_{c\lambda,N+1}$ can be regarded as a function of the general coupling force $\bar{\lambda}^*_{c,N+1}$

$$\begin{aligned} \bar{g}^B_{c\lambda,N+1}(\bar{\lambda}^*_{c,N+1}) := &\left(\bar{x}^*_{2,N+1}\left(\bar{\lambda}^*_{c,N+1}\right) - \bar{x}^*_{1,N+1}\left(\bar{\lambda}^*_{c,N+1}\right)\right) \\ &+ \bar{\beta} \cdot \left(\bar{v}^*_{2,N+1}\left(\bar{\lambda}^*_{c,N+1}\right) - \bar{v}^*_{1,N+1}\left(\bar{\lambda}^*_{c,N+1}\right)\right) + \bar{\gamma} \cdot \left(\bar{v}'^*_{2,N+1}\left(\bar{\lambda}^*_{c,N+1}\right) - \bar{v}'^*_{1,N+1}\left(\bar{\lambda}^*_{c,N+1}\right)\right). \end{aligned} \tag{14}$$

Since the state variables $\bar{x}^*_{1,N+1}$, $\bar{x}^*_{2,N+1}$, $\bar{v}^*_{1,N+1}$, $\bar{v}^*_{2,N+1}$ and the accelerations $\bar{v}'^*_{1,N+1}$, $\bar{v}'^*_{2,N+1}$ depend only linearly on $\bar{\lambda}^*_{c,N+1}$, Eq. (14) can be rewritten as

$$\begin{aligned}
\bar{g}^B_{c\lambda,N+1}(\bar{\lambda}^*_{c,N+1}) &:= \bar{g}^B_{c\lambda,N+1}(\bar{\lambda}^p_{c,N+1}) + \left.\frac{\partial \bar{g}^B_{c\lambda,N+1}}{\partial \bar{\lambda}^*_{c,N+1}}\right|_{\bar{\lambda}^p_{c,N+1}} \cdot (\bar{\lambda}^*_{c,N+1} - \bar{\lambda}^p_{c,N+1}) \\
&= \left(\bar{x}^p_{2,N+1} - \bar{x}^p_{1,N+1}\right) + \bar{\beta} \cdot \left(\bar{v}^p_{2,N+1} - \bar{v}^p_{1,N+1}\right) + \bar{\gamma} \cdot \left(\bar{v}'^p_{2,N+1} - \bar{v}'^p_{1,N+1}\right) \\
&\quad + \left[\left(\left.\frac{\partial \bar{x}^*_{2,N+1}}{\partial \bar{\lambda}^*_{c,N+1}}\right|_{\bar{\lambda}^p_{c,N+1}} - \left.\frac{\partial \bar{x}^*_{1,N+1}}{\partial \bar{\lambda}^*_{c,N+1}}\right|_{\bar{\lambda}^p_{c,N+1}} \right) \right. \\
&\quad + \bar{\beta} \cdot \left(\left.\frac{\partial \bar{v}^*_{2,N+1}}{\partial \bar{\lambda}^*_{c,N+1}}\right|_{\bar{\lambda}^p_{c,N+1}} - \left.\frac{\partial \bar{v}^*_{1,N+1}}{\partial \bar{\lambda}^*_{c,N+1}}\right|_{\bar{\lambda}^p_{c,N+1}} \right) \\
&\quad \left. + \bar{\gamma} \cdot \left(\left.\frac{\partial \bar{v}'^*_{2,N+1}}{\partial \bar{\lambda}^*_{c,N+1}}\right|_{\bar{\lambda}^p_{c,N+1}} - \left.\frac{\partial \bar{v}'^*_{1,N+1}}{\partial \bar{\lambda}^*_{c,N+1}}\right|_{\bar{\lambda}^p_{c,N+1}} \right) \right] \cdot (\bar{\lambda}^*_{c,N+1} - \bar{\lambda}^p_{c,N+1}),
\end{aligned} \tag{15}$$

where $\bar{\lambda}^p_{c,N+1} = \bar{\lambda}^p_c(\bar{T}_{N+1})$ terms the predicted coupling force at $\bar{T}_{N+1}$.

- By setting $\bar{g}^B_{c\lambda,N+1}(\bar{\lambda}^*_{c,N+1}) = 0$, one obtains the corrected coupling force

$$\begin{aligned}
\bar{\lambda}_{c,N+1} &= \bar{\lambda}^p_{c,N+1} \\
&\quad - \frac{\left(\bar{x}^p_{2,N+1} - \bar{x}^p_{1,N+1}\right) + \bar{\beta} \cdot \left(\bar{v}^p_{2,N+1} - \bar{v}^p_{1,N+1}\right) + \cdots}{\left[\left(\left.\frac{\partial \bar{x}^*_{2,N+1}}{\partial \bar{\lambda}^*_{c,N+1}}\right|_{\bar{\lambda}^p_{c,N+1}} - \left.\frac{\partial \bar{x}^*_{1,N+1}}{\partial \bar{\lambda}^*_{c,N+1}}\right|_{\bar{\lambda}^p_{c,N+1}} \right) + \bar{\beta} \cdot \left(\left.\frac{\partial \bar{v}^*_{2,N+1}}{\partial \bar{\lambda}^*_{c,N+1}}\right|_{\bar{\lambda}^p_{c,N+1}} - \left.\frac{\partial \bar{v}^*_{1,N+1}}{\partial \bar{\lambda}^*_{c,N+1}}\right|_{\bar{\lambda}^p_{c,N+1}} \right) + \cdots \right]}.
\end{aligned} \tag{16}$$

  For the reason of a precise representation, we use different variables for the general coupling force $\bar{\lambda}^*_{c,N+1}$ at the time point $\bar{T}_{N+1}$ and the corrected coupling force $\bar{\lambda}_{c,N+1}$, which represents the root of Eq. (15).

Step 3: Corrector Step

- Analytically integrating subsystem 1 and subsystem 2 from $\bar{T}_N$ to $\bar{T}_{N+1}$ with the initial conditions (8a) and using an interpolation polynomial with the corrected coupling force $\bar{\lambda}_{c,N+1}$ of Eq. (16), yields the corrected states

$$\bar{x}_{1,N+1}, \quad \bar{v}_{1,N+1} \quad \text{and} \quad \bar{x}_{2,N+1}, \quad \bar{v}_{2,N+1}, \tag{17}$$

  which are functions of $\bar{\lambda}_{c,N+1}, \bar{\lambda}_{c,N}, \ldots, \bar{\lambda}_{c,N-k+1}, \boldsymbol{z}_N$.

In Eq. (16), the predicted acceleration variables can easily be eliminated with the help of Eqs. (7a) and (7b), i.e. by means of

$$\begin{aligned}
\bar{v}'^p_{1,N+1} &= -\bar{c}_1 \cdot \bar{x}^p_{1,N+1} - \bar{d}_1 \cdot \bar{v}^p_{1,N+1} + \bar{\lambda}^p_{c,N+1}, \\
\bar{v}'^p_{2,N+1} &= -\frac{\alpha_{c21}}{\alpha_{m21}} \cdot \bar{c}_1 \cdot \bar{x}^p_{2,N+1} - \frac{\alpha_{d21}}{\alpha_{m21}} \cdot \bar{d}_1 \cdot \bar{v}^p_{2,N+1} - \frac{1}{\alpha_{m21}} \cdot \bar{\lambda}^p_{c,N+1}.
\end{aligned} \tag{18}$$

Furthermore, the predicted position and velocity variables can be replaced with the help of Eq. (10) and the predicted Lagrange multiplier by means of Eq. (9), so that Eq. (16) finally results in a relationship of the form

$$\bar{\lambda}_{c,N+1} = \bar{\lambda}_{c,N+1}\left(\bar{\lambda}_{c,N}, \bar{\lambda}_{c,N-1}, \ldots, \bar{\lambda}_{c,N-k}, \boldsymbol{z}_N\right). \tag{19}$$

Combining Eq. (17) and Eq. (19) yields the governing system of recurrence equations

$$\begin{aligned}
\bar{x}_{1,N+1} &= \bar{x}_{1,N+1}\left(\bar{\lambda}_{c,N+1}, \bar{\lambda}_{c,N}, \ldots, \bar{\lambda}_{c,N-k+1}, \boldsymbol{z}_N\right), \\
\bar{v}_{1,N+1} &= \bar{v}_{1,N+1}\left(\bar{\lambda}_{c,N+1}, \bar{\lambda}_{c,N}, \ldots, \bar{\lambda}_{c,N-k+1}, \boldsymbol{z}_N\right), \\
\bar{x}_{2,N+1} &= \bar{x}_{2,N+1}\left(\bar{\lambda}_{c,N+1}, \bar{\lambda}_{c,N}, \ldots, \bar{\lambda}_{c,N-k+1}, \boldsymbol{z}_N\right), \\
\bar{v}_{2,N+1} &= \bar{v}_{2,N+1}\left(\bar{\lambda}_{c,N+1}, \bar{\lambda}_{c,N}, \ldots, \bar{\lambda}_{c,N-k+1}, \boldsymbol{z}_N\right), \\
\bar{\lambda}_{c,N+1} &= \bar{\lambda}_{c,N+1}\left(\bar{\lambda}_{c,N}, \bar{\lambda}_{c,N-1}, \ldots, \bar{\lambda}_{c,N-k}, \boldsymbol{z}_N\right)
\end{aligned} \tag{20}$$

for the state variables and the Lagrange multiplier of the discretized co-simulation test-model. Eq. (20) represents a system of 5 coupled linear recurrence equations of order $k+1$. Introducing the vectors $\hat{\boldsymbol{z}}_{N+1} = (\bar{x}_{1,N+1}, \bar{v}_{1,N+1}, \bar{x}_{2,N+1}, \bar{v}_{2,N+1}, \bar{\lambda}_{c,N+1})^T \in \mathbb{R}^5$, $\hat{\boldsymbol{z}}_N = \cdots$, etc., which collect the state variables of both subsystems and the Lagrange multiplier at the macro-time points, Eq. (20) can symbolically be written as

$$\boldsymbol{A}_{N+1} \cdot \hat{\boldsymbol{z}}_{N+1} + \boldsymbol{A}_N \cdot \hat{\boldsymbol{z}}_N + \cdots + \boldsymbol{A}_{N-k} \cdot \hat{\boldsymbol{z}}_{N-k} = \boldsymbol{0}. \tag{21}$$

The real-valued matrices $\boldsymbol{A}_{N+1}, \ldots, \boldsymbol{A}_{N-k} \in \mathbb{R}^{5\times 5}$ are constant and depend only on the 5 parameters of the co-simulation test model, see Eq. (5). It should be stressed again that the subsystems are integrated analytically. This is possible, because the co-simulation test model is linear. Hence, the stability behavior of the system of recurrence equations (21) directly reflects (defines) the stability of the underlying co-simulation approach. Stabilizing or destabilizing effects due to numerical subsystem integration are not present in the current analysis. The stability of the homogenous linear system of recurrence equations (21) can easiliy be determined by an eigenvalue analysis. The homogenous solution of Eq. (21) is obtained by making use of the exponential approach $\hat{\boldsymbol{z}}_N = \boldsymbol{Z} \cdot \lambda^N$, where λ terms an eigenvalue and $\boldsymbol{Z}$ an eigenvector of the recurrence system. Inserting the exponential approach into Eq. (21) yields

$$\left(\boldsymbol{A}_{N+1} \cdot \lambda^{N+1} + \boldsymbol{A}_N \cdot \lambda^N + \cdots + \boldsymbol{A}_{N-k} \cdot \lambda^{N-k}\right) \boldsymbol{Z} = \boldsymbol{0}. \tag{22}$$

The homogenous linear system of equations (22) has nontrivial solutions, if

$$det\left(\boldsymbol{A}_{N+1} \cdot \lambda^{k+1} + \boldsymbol{A}_N \cdot \lambda^k + \cdots + \boldsymbol{A}_{N-k}\right) = 0. \tag{23}$$

Eq. (23) is the characteristic equation of the recurrence system (21) and represents a polynomial of order $5 \cdot (k+1)$ in λ. The zeros of the characteristic equation are the eigenvalues λ_j, $j = 1, \ldots, 5 \cdot (k+1)$. The recurrence system (21) is stable, if the magnitude $|\lambda_j|$ of all eigenvalues is smaller than 1. Hence, the recurrence system and in consequence the underlying co-simulation approach get unstable, if the spectral radius $\rho = \max\{|\lambda_j|\}$ – that means the magnitude of the largest eigenvalue – is larger than 1. Note that the spectral radius ρ is only a function of the 5 independent parameters defined in Eq. (5).

Finally, it should be mentioned that the implicit co-simulation approach presented above only requires one corrector step, since the test model is linear and the gradients, see Eq. (13), for the corrector step are constant. Considering general nonlinear problems, the proposed 3-stage predictor/corrector approach represents a semi-implicit method, see Ref. [34]. In order to get a fully implicit approach for non-linear problems, a corrector iteration with several corrector steps has to be carried out.

2.1.2 Implicit co-simulation method based on weighted multiplier approach

The second method analyzed in this manuscript is called weighted multiplier approach. For a detailed description of this method, we refer to Ref. [34]. The weighted multiplier approach is very similar to the Baumgarte co-simulation method of Sect. 2.1.1. Only step 2 has to be slightly modified.

Step 1: Predictor Step

- Identical with step 1 in Sect. 2.1.1.

Step 2: Calculation of Corrected Coupling Force

- Instead of using the corrected coupling force according to Eq. (16), the following corrected coupling force is applied

$$\bar{\lambda}_{c,N+1} = \bar{\lambda}^{p}_{c,N+1} - \frac{1}{1+a+b} \cdot \left[\frac{\left(\bar{x}^{p}_{2,N+1} - \bar{x}^{p}_{1,N+1}\right)}{\left(\left.\frac{\partial \bar{x}^{*}_{2,N+1}}{\partial \bar{\lambda}^{*}_{c,N+1}}\right|_{\bar{\lambda}^{p}_{c,N+1}} - \left.\frac{\partial \bar{x}^{*}_{1,N+1}}{\partial \bar{\lambda}^{*}_{c,N+1}}\right|_{\bar{\lambda}^{p}_{c,N+1}} \right)} \right.$$

$$\left. + a \cdot \frac{\left(\bar{v}^{p}_{2,N+1} - \bar{v}^{p}_{1,N+1}\right)}{\left(\left.\frac{\partial \bar{v}^{*}_{2,N+1}}{\partial \bar{\lambda}^{*}_{c,N+1}}\right|_{\bar{\lambda}^{p}_{c,N+1}} - \left.\frac{\partial \bar{v}^{*}_{1,N+1}}{\partial \bar{\lambda}^{*}_{c,N+1}}\right|_{\bar{\lambda}^{p}_{c,N+1}} \right)} + b \cdot \frac{\left(\bar{v}'^{p}_{2,N+1} - \bar{v}'^{p}_{1,N+1}\right)}{\left(\left.\frac{\partial \bar{v}'^{*}_{2,N+1}}{\partial \bar{\lambda}^{*}_{c,N+1}}\right|_{\bar{\lambda}^{p}_{c,N+1}} - \left.\frac{\partial \bar{v}'^{*}_{1,N+1}}{\partial \bar{\lambda}^{*}_{c,N+1}}\right|_{\bar{\lambda}^{p}_{c,N+1}} \right)} \right]. \tag{24}$$

The real-valued parameters $a > 0$ and $b > 0$ have to be specified by the user (e.g. $a = b = 1$).

- The physical interpretation of the weighted multiplier approach is straightforward. Calculation of a corrected coupling force based on the constraint equation $\bar{g}^{pos}_{c\lambda} := \bar{x}_2 - \bar{x}_1 = 0$ on position level (instead of the Baumgarte function (7c)), yields the corrected coupling force

$$\bar{\lambda}^{pos}_{c,N+1} = \bar{\lambda}^{p}_{c,N+1} - \frac{\left(\bar{x}^{p}_{2,N+1} - \bar{x}^{p}_{1,N+1}\right)}{\left(\left.\frac{\partial \bar{x}^{*}_{2,N+1}}{\partial \bar{\lambda}^{*}_{c,N+1}}\right|_{\bar{\lambda}^{p}_{c,N+1}} - \left.\frac{\partial \bar{x}^{*}_{1,N+1}}{\partial \bar{\lambda}^{*}_{c,N+1}}\right|_{\bar{\lambda}^{p}_{c,N+1}} \right)}. \tag{25}$$

- Analogously, by using the constraint equation $\bar{g}^{vel}_{c\lambda} := \bar{v}_2 - \bar{v}_1 = 0$ on velocity level, the corrected coupling force is given by

$$\bar{\lambda}^{vel}_{c,N+1} = \bar{\lambda}^{p}_{c,N+1} - \frac{\left(\bar{v}^{p}_{2,N+1} - \bar{v}^{p}_{1,N+1}\right)}{\left(\left.\frac{\partial \bar{v}^{*}_{2,N+1}}{\partial \bar{\lambda}^{*}_{c,N+1}}\right|_{\bar{\lambda}^{p}_{c,N+1}} - \left.\frac{\partial \bar{v}^{*}_{1,N+1}}{\partial \bar{\lambda}^{*}_{c,N+1}}\right|_{\bar{\lambda}^{p}_{c,N+1}} \right)}. \tag{26}$$

- Applying the constraint equation $\bar{g}^{acc}_{c\lambda} := \bar{v}'_2 - \bar{v}'_1 = 0$ on acceleration level results in the corrected coupling force

$$\bar{\lambda}^{acc}_{c,N+1} = \bar{\lambda}^{p}_{c,N+1} - \frac{\left(\bar{v}'^{p}_{2,N+1} - \bar{v}'^{p}_{1,N+1}\right)}{\left(\left.\frac{\partial \bar{v}'^{*}_{2,N+1}}{\partial \bar{\lambda}^{*}_{c,N+1}}\right|_{\bar{\lambda}^{p}_{c,N+1}} - \left.\frac{\partial \bar{v}'^{*}_{1,N+1}}{\partial \bar{\lambda}^{*}_{c,N+1}}\right|_{\bar{\lambda}^{p}_{c,N+1}} \right)}. \tag{27}$$

- Hence, the corrected coupling force $\bar{\lambda}_{c,N+1}$ defined in Eq. (24) is simply the weighted sum of $\bar{\lambda}^{pos}_{c,N+1}$, $\bar{\lambda}^{vel}_{c,N+1}$ and $\bar{\lambda}^{acc}_{c,N+1}$.

Step 3: Corrector Step

- As step 3 in Section 2.1.1, however the corrected coupling force $\bar{\lambda}_{c,N+1}$ according to Eq. (24) is used instead of $\bar{\lambda}_{c,N+1}$ from Eq. (16).

Using the weighted multiplier approach also yields a linear system of recurrence equations of order $k+1$ with the same structure as Eq. (21). The matrices $\boldsymbol{A}_N, \ldots, \boldsymbol{A}_{N-k}$ for the weighted multiplier approach are however different from the corresponding matrices of the Baumgarte method.

2.1.3 Implicit co-simulation method based on projection technique

The third method investigated in this paper is based on a classical projection approach, which is well-established in the field of DAE theory [22]. The implicit co-simulation method based on the projection technique is carried out in four steps.

Step 1: Predictor Step

- Identical with step 1 in Sect. 2.1.1.

Step 2: Calculation of Corrected Coupling Force

- Identical with step 2 in Sect. 2.1.1 with one exception: Instead of calculating the corrected coupling force according to Eq. (16), the corrected coupling force $\bar{\lambda}_{c,N+1}^{acc}$ according to Eq. (27) is applied.

Step 3: Corrector Step

- As step 3 in Sect. 2.1.1, however $\bar{\lambda}_{c,N+1} = \bar{\lambda}_{c,N+1}^{acc}$ is used as corrected coupling force. The result are the corrected state variables

$$\bar{x}_{1,N+1}, \quad \bar{v}_{1,N+1} \quad \text{and} \quad \bar{x}_{2,N+1}, \quad \bar{v}_{2,N+1}, \tag{28}$$

  which are depending on $\bar{\lambda}_{c,N+1}, \bar{\lambda}_{c,N}, \ldots, \bar{\lambda}_{c,N-k+1}, \boldsymbol{z}_N$.
- Eliminating the predicted acceleration variables in Eq. (27) with the help of Eq. (18) and making furthermore use of Eq. (10) and Eq. (9), Eq. (27) finally results in a relationship of the form

$$\bar{\lambda}_{c,N+1} = \bar{\lambda}_{c,N+1}\left(\bar{\lambda}_{c,N}, \bar{\lambda}_{c,N-1}, \ldots, \bar{\lambda}_{c,N-k}, \boldsymbol{z}_N\right). \tag{29}$$

Step 4: Projection Step

- Calculation of projected position and velocity variables according to Ref. [22] gives

$$\bar{x}_{N+1} = \frac{\bar{x}_{1,N+1} + \alpha_{m21} \cdot \bar{x}_{2,N+1}}{1 + \alpha_{m21}}, \quad \bar{v}_{N+1} = \frac{\bar{v}_{1,N+1} + \alpha_{m21} \cdot \bar{v}_{2,N+1}}{1 + \alpha_{m21}}. \tag{30}$$

Eq. (30) together with Eq. (29) represent a system of 3 coupled linear recurrence equations of order $k+1$. Now, it should be recognized again that the vector $\boldsymbol{z}_N$ represents the initial conditions for the macro-time step $\bar{T}_N \to \bar{T}_{N+1}$. Since a projection step has also been carried out at the macro-time point $\bar{T}_N$, we have $\boldsymbol{z}_N = (\bar{x}_{1,N}, \bar{v}_{1,N}, \bar{x}_{2,N}, \bar{v}_{2,N})^T = (\bar{x}_N, \bar{v}_N, \bar{x}_N, \bar{v}_N)^T$. Hence, the governing linear system of recurrence equations for the projected state variables $\bar{x}_{N+1}$, $\bar{v}_{N+1}$ and for the Lagrange multiplier $\bar{\lambda}_{c,N+1}$ has the following structure

$$\begin{aligned}
\bar{x}_{N+1} &= \bar{x}_{N+1}\left(\bar{\lambda}_{c,N+1}, \bar{\lambda}_{c,N}, \ldots, \bar{\lambda}_{c,N-k+1}, \bar{x}_N, \bar{v}_N\right), \\
\bar{v}_{N+1} &= \bar{v}_{N+1}\left(\bar{\lambda}_{c,N+1}, \bar{\lambda}_{c,N}, \ldots, \bar{\lambda}_{c,N-k+1}, \bar{x}_N, \bar{v}_N\right), \\
\bar{\lambda}_{c,N+1} &= \bar{\lambda}_{c,N+1}\left(\bar{\lambda}_{c,N}, \bar{\lambda}_{c,N-1}, \ldots, \bar{\lambda}_{c,N-k}, \bar{x}_N, \bar{v}_N\right).
\end{aligned} \tag{31}$$

Introducing the vectors $\hat{\boldsymbol{y}}_{N+1} = (\bar{x}_{N+1}, \bar{v}_{N+1}, \bar{\lambda}_{c,N+1})^T \in \mathbb{R}^3$, $\hat{\boldsymbol{y}}_N = \cdots$, etc., which collect the projected state variables and the Lagrange multiplier at the macro-time points, Eq. (31) can symbolically be written as

$$\boldsymbol{B}_{N+1} \cdot \hat{\boldsymbol{y}}_{N+1} + \boldsymbol{B}_N \cdot \hat{\boldsymbol{y}}_N + \cdots + \boldsymbol{B}_{N-k} \cdot \hat{\boldsymbol{y}}_{N-k} = \boldsymbol{0}. \tag{32}$$

The real-valued matrices $\boldsymbol{B}_{N+1}, \ldots, \boldsymbol{B}_{N-k} \in \mathbb{R}^{3\times 3}$ are constant and only depend on the 5 parameters of the co-simulation test model.

2.2 Force/Displacement-coupling

2.2.1 Implicit co-simulation method based on baumgarte stabilization

If the co-simulation test model is decomposed by a force/displacement-coupling approach [36], subsystem 1 will be a force-driven single-mass oscillator and subsystem 2 a kinematically driven single-mass oscillator, see Fig. 3. The kinematical motion for the mass m_2 can be applied on position (index-3), velocity (index-2) or acceleration (index-1) level. Here, the motion is applied on index-1 level for stability reasons, i.e. the acceleration of the mass m_2 is prescribed by a rheonomic constraint equation. Since the two masses are coupled by a rigid link, the motion (acceleration) of both masses has to be identical. Consequently, the kinematical motion for the mass m_2 is defined by the motion of the mass m_1, i.e. the acceleration of m_2 is prescribed by the acceleration of m_1. Since the acceleration $\bar{v}_1'$ of mass m_1 is unknown in subsystem 2, the additional coupling variable $\tilde{\bar{a}}_1(t)$ has to be defined. Introducing an additional coupling variable requires the definition

of an additional coupling condition, namely $\bar{g}_{c\mu} := \bar{\mu}_2 - \bar{\lambda}_c = 0$, which states that the coupling forces are equal in both subsystems.

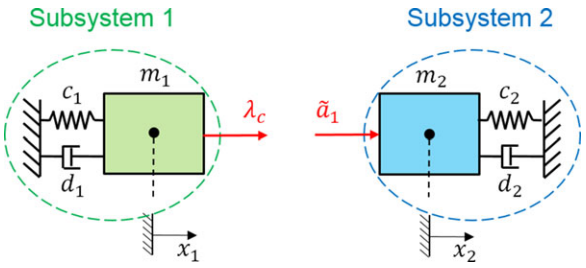

Fig. 3 Co-simulation test model: force/displacement-decomposition approach.

The decomposed system is described by the subsequent DAE system

Subsystem 1:

$$\bar{x}_1' = \bar{v}_1, \qquad \bar{v}_1' = -\bar{c}_1 \cdot \bar{x}_1 - \bar{d}_1 \cdot \bar{v}_1 + \bar{\lambda}_c, \tag{33a}$$

Subsystem 2:

$$\bar{x}_2' = \bar{v}_2, \qquad \bar{v}_2' = -\frac{\alpha_{c21}}{\alpha_{m21}} \cdot \bar{c}_1 \cdot \bar{x}_2 - \frac{\alpha_{d21}}{\alpha_{m21}} \cdot \bar{d}_1 \cdot \bar{v}_2 - \frac{1}{\alpha_{m21}} \cdot \bar{\mu}_2,$$
$$\bar{v}_2' - \tilde{\bar{a}}_1 = 0, \tag{33b}$$

Coupling conditions:

$$\bar{g}_{c\lambda}^B := (\bar{x}_2 - \bar{x}_1) + \bar{\beta} \cdot (\bar{v}_2 - \bar{v}_1) + \bar{\gamma} \cdot (\bar{v}_2' - \bar{v}_1') = 0,$$
$$\bar{g}_{c\mu} := \bar{\mu}_2 - \bar{\lambda}_c = 0. \tag{33c}$$

Note that $\bar{\mu}_2$ terms a Lagrange multiplier, which is introduced to realize the rheonomic constraint equation $\bar{v}_2' - \tilde{\bar{a}}_1 = 0$ in subsystem 2, where $\tilde{\bar{a}}_1(t)$ represents the applied motion for m_2. To derive the governing system of recurrence equations for the Baumgarte method on the basis of a force/displacement-decomposition approach, we consider again the general macro-step from $\bar{T}_N$ to $\bar{T}_{N+1}$. As in Sect. 2.1, we ride on the assumption that at the beginning of the macro-time step, the state vectors, the Lagrange multiplier $\bar{\mu}_2$ and the coupling variables $\bar{\lambda}_c, \tilde{\bar{a}}_1$ are known

$$\bar{x}_1\left(\bar{T}_N\right) = \bar{x}_{1,N}, \qquad \bar{v}_1\left(\bar{T}_N\right) = \bar{v}_{1,N},$$
$$\bar{x}_2\left(\bar{T}_N\right) = \bar{x}_{2,N}, \qquad \bar{v}_2\left(\bar{T}_N\right) = \bar{v}_{2,N}, \qquad \bar{\mu}_2\left(\bar{T}_N\right) = \bar{\mu}_{2,N}, \tag{34a}$$
$$\bar{\lambda}_c\left(\bar{T}_N\right) = \bar{\lambda}_{c,N}, \qquad \tilde{\bar{a}}_1\left(\bar{T}_N\right) = \tilde{\bar{a}}_{1,N}. \tag{34b}$$

For higher order approximation ($k > 0$), the corresponding variables at the previous macro-time points are also assumed to be known.

Step 1: Predictor Step

- Integrating subsystem 1 and subsystem 2 from $\bar{T}_N$ to $\bar{T}_{N+1}$ with the initial conditions (34a) and with the predictor (extrapolation) polynomials

$$\bar{\lambda}_c^p(\bar{t}) = P_{\bar{\lambda}_c}^p\left[\left(\bar{T}_N, \bar{\lambda}_{c,N}\right), \left(\bar{T}_{N-1}, \bar{\lambda}_{c,N-1}\right), \ldots, \left(\bar{T}_{N-k}, \bar{\lambda}_{c,N-k}\right); \bar{t}\right],$$
$$\tilde{\bar{a}}_1^p(\bar{t}) = P_{\tilde{\bar{a}}_1}^p\left[\left(\bar{T}_N, \tilde{\bar{a}}_{1,N}\right), \left(\bar{T}_{N-1}, \tilde{\bar{a}}_{1,N-1}\right), \ldots, \left(\bar{T}_{N-k}, \tilde{\bar{a}}_{1,N-k}\right); \bar{t}\right], \tag{35}$$

yields the predicted state variables and the predicted Lagrange multiplier at the macro-time point $\bar{T}_{N+1}$, i.e.

$$\bar{x}_{1,N+1}^p, \quad \bar{v}_{1,N+1}^p \quad \text{and} \quad \bar{x}_{2,N+1}^p, \quad \bar{v}_{2,N+1}^p, \quad \bar{\mu}_{2,N+1}^p. \tag{36}$$

It should be pointed out that $\bar{x}_{1,N+1}^p$ and $\bar{v}_{1,N+1}^p$ are functions of $\bar{\lambda}_{c,N}, \bar{\lambda}_{c,N-1}, \ldots, \bar{\lambda}_{c,N-k}, z_N$, whereas $\bar{x}_{2,N+1}^p$, $\bar{v}_{2,N+1}^p$ and $\bar{\mu}_{2,N+1}^p$ depend on $\tilde{\bar{a}}_{1,N}, \tilde{\bar{a}}_{1,N-1}, \ldots, \tilde{\bar{a}}_{1,N-k}, z_N$.

Step 2: Calculation of Corrected Coupling Variables

- An integration of subsystem 1 and subsystem 2 from $\bar{T}_N$ to $\bar{T}_{N+1}$ with the initial conditions (34a) and with the interpolation polynomials

$$\begin{aligned}\bar{\lambda}_c^*(\bar{t}) &= P^*_{\bar{\lambda}_c}\left[\left(\bar{T}_{N+1}, \bar{\lambda}^*_{c,N+1}\right), \left(\bar{T}_N, \bar{\lambda}_{c,N}\right), \ldots, \left(\bar{T}_{N-k+1}, \bar{\lambda}_{c,N-k+1}\right); \bar{t}\right], \\ \tilde{a}_1^*(\bar{t}) &= P^*_{\tilde{a}_1}\left[\left(\bar{T}_{N+1}, \tilde{a}^*_{1,N+1}\right), \left(\bar{T}_N, \tilde{a}_{1,N}\right), \ldots, \left(\bar{T}_{N-k+1}, \tilde{a}_{1,N-k+1}\right); \bar{t}\right],\end{aligned} \tag{37}$$

gives the following state variables and Lagrange multiplier at the macro-time point $\bar{T}_{N+1}$

$$\bar{x}^*_{1,N+1}, \quad \bar{v}^*_{1,N+1} \quad \text{and} \quad \bar{x}^*_{2,N+1}, \quad \bar{v}^*_{2,N+1}, \quad \bar{\mu}^*_{2,N+1}. \tag{38}$$

Note that $\bar{x}^*_{1,N+1}$ and $\bar{v}^*_{1,N+1}$ are depending on $\bar{\lambda}^*_{c,N+1}, \bar{\lambda}_{c,N}, \ldots, \bar{\lambda}_{c,N-k+1}, \boldsymbol{z}_N$, while $\bar{x}^*_{2,N+1}, \bar{v}^*_{2,N+1}$ and $\bar{\mu}^*_{2,N+1}$ are functions of $\tilde{a}^*_{1,N+1}, \tilde{a}_{1,N}, \ldots, \tilde{a}_{1,N-k+1}, \boldsymbol{z}_N$. It should be mentioned that $\bar{\lambda}^*_{c,N+1}$ and $\tilde{a}^*_{1,N+1}$ represent arbitrary coupling variables at the macro-time point $\bar{T}_{N+1}$.
- Differentiating the state variables and the Lagrange multiplier of Eq. (38) with respect to $\bar{\lambda}^*_{c,N+1}$ and $\tilde{a}^*_{1,N+1}$, we get the following partial derivatives

$$\begin{aligned}&\frac{\partial \bar{x}^*_{1,N+1}}{\partial \bar{\lambda}^*_{c,N+1}} = const., \quad \frac{\partial \bar{v}^*_{1,N+1}}{\partial \bar{\lambda}^*_{c,N+1}} = const., \quad \frac{\partial \bar{v}'^*_{1,N+1}}{\partial \bar{\lambda}^*_{c,N+1}} = const., \\ &\frac{\partial \bar{x}^*_{2,N+1}}{\partial \tilde{a}^*_{1,N+1}} = const., \quad \frac{\partial \bar{v}^*_{2,N+1}}{\partial \tilde{a}^*_{1,N+1}} = const., \quad \frac{\partial \bar{v}'^*_{2,N+1}}{\partial \tilde{a}^*_{1,N+1}} = const., \quad \frac{\partial \bar{\mu}^*_{2,N+1}}{\partial \tilde{a}^*_{1,N+1}} = const..\end{aligned} \tag{39}$$

- Regarding the fixed macro-time point $\bar{T}_{N+1}$, the coupling conditions $\bar{g}^B_{c\lambda,N+1}$ and $\bar{g}_{c\mu,N+1}$ can be considered as functions of the general coupling variables $\bar{\lambda}^*_{c,N+1}$ and $\tilde{a}^*_{1,N+1}$, i.e.

$$\begin{aligned}\bar{g}^B_{c\lambda,N+1}\left(\bar{\lambda}^*_{c,N+1}, \tilde{a}^*_{1,N+1}\right) &:= \left(\bar{x}^*_{2,N+1}\left(\tilde{a}^*_{1,N+1}\right) - \bar{x}^*_{1,N+1}\left(\bar{\lambda}^*_{c,N+1}\right)\right) + \bar{\beta} \cdot \left(\bar{v}^*_{2,N+1}\left(\tilde{a}^*_{1,N+1}\right) - \bar{v}^*_{1,N+1}\left(\bar{\lambda}^*_{c,N+1}\right)\right) \\ &\quad + \bar{\gamma} \cdot \left(\bar{v}'^*_{2,N+1}\left(\tilde{a}^*_{1,N+1}\right) - \bar{v}'^*_{1,N+1}\left(\bar{\lambda}^*_{c,N+1}\right)\right), \\ \bar{g}_{c\mu,N+1}\left(\bar{\lambda}^*_{c,N+1}, \tilde{a}^*_{1,N+1}\right) &:= \bar{\mu}^*_{2,N+1}\left(\tilde{a}^*_{1,N+1}\right) - \bar{\lambda}^*_{c,N+1}.\end{aligned} \tag{40}$$

Since the test-model is linear, the state variables $\bar{x}^*_{1,N+1}, \bar{x}^*_{2,N+1}, \bar{v}^*_{1,N+1}, \bar{v}^*_{2,N+1}$, the accelerations $\bar{v}'^*_{1,N+1}, \bar{v}'^*_{2,N+1}$ and the Lagrange multiplier $\bar{\mu}^*_{2,N+1}$ are linear functions of the coupling variables $\bar{\lambda}^*_{c,N+1}$ and $\tilde{a}^*_{1,N+1}$. Hence, the coupling conditions can be expressed as

$$\begin{aligned}\bar{g}^B_{c\lambda,N+1}(\bar{\lambda}^*_{c,N+1}, \tilde{a}^*_{1,N+1}) &:= \bar{g}^B_{c\lambda,N+1}(\boldsymbol{e}^p) + \left.\frac{\partial \bar{g}^B_{c\lambda,N+1}}{\partial \bar{\lambda}^*_{c,N+1}}\right|_{\boldsymbol{e}^p} \cdot \left(\bar{\lambda}^*_{c,N+1} - \bar{\lambda}^p_{c,N+1}\right) \\ &\quad + \left.\frac{\partial \bar{g}^B_{c\lambda,N+1}}{\partial \tilde{a}^*_{1,N+1}}\right|_{\boldsymbol{e}^p} \cdot \left(\tilde{a}^*_{1,N+1} - \tilde{a}^p_{1,N+1}\right) \\ &= \left(\bar{x}^p_{2,N+1} - \bar{x}^p_{1,N+1}\right) + \bar{\beta} \cdot \left(\bar{v}^p_{2,N+1} - \bar{v}^p_{1,N+1}\right) + \bar{\gamma} \cdot \left(\bar{v}'^p_{2,N+1} - \bar{v}'^p_{1,N+1}\right) \\ &\quad - \left[\left.\frac{\partial \bar{x}^*_{1,N+1}}{\partial \bar{\lambda}^*_{c,N+1}}\right|_{\boldsymbol{e}^p} + \bar{\beta} \cdot \left.\frac{\partial \bar{v}^*_{1,N+1}}{\partial \bar{\lambda}^*_{c,N+1}}\right|_{\boldsymbol{e}^p} + \bar{\gamma} \cdot \left.\frac{\partial \bar{v}'^*_{1,N+1}}{\partial \bar{\lambda}^*_{c,N+1}}\right|_{\boldsymbol{e}^p}\right] \cdot \left(\bar{\lambda}^*_{c,N+1} - \bar{\lambda}^p_{c,N+1}\right) \\ &\quad + \left[\left.\frac{\partial \bar{x}^*_{2,N+1}}{\partial \tilde{a}^*_{1,N+1}}\right|_{\boldsymbol{e}^p} + \bar{\beta} \cdot \left.\frac{\partial \bar{v}^*_{2,N+1}}{\partial \tilde{a}^*_{1,N+1}}\right|_{\boldsymbol{e}^p} + \bar{\gamma} \cdot \left.\frac{\partial \bar{v}'^*_{2,N+1}}{\partial \tilde{a}^*_{1,N+1}}\right|_{\boldsymbol{e}^p}\right] \cdot \left(\tilde{a}^*_{1,N+1} - \tilde{a}^p_{1,N+1}\right),\end{aligned} \tag{41}$$

$$\begin{aligned}\bar{g}_{c\mu,N+1}\left(\bar{\lambda}^*_{c,N+1}, \tilde{a}^*_{1,N+1}\right) &:= \bar{g}_{c\mu,N+1}(\boldsymbol{e}^p) + \left.\frac{\partial \bar{g}_{c\mu,N+1}}{\partial \bar{\lambda}^*_{c,N+1}}\right|_{\boldsymbol{e}^p} \cdot \left(\bar{\lambda}^*_{c,N+1} - \bar{\lambda}^p_{c,N+1}\right) \\ &\quad + \left.\frac{\partial \bar{g}_{c\mu,N+1}}{\partial \tilde{a}^*_{1,N+1}}\right|_{\boldsymbol{e}^p} \cdot \left(\tilde{a}^*_{1,N+1} - \tilde{a}^p_{1,N+1}\right) \\ &= \bar{\mu}^p_{2,N+1} - \bar{\lambda}^p_{c,N+1} - 1 \cdot \left(\bar{\lambda}^*_{c,N+1} - \bar{\lambda}^p_{c,N+1}\right) + \left.\frac{\partial \bar{\mu}^*_{2,N+1}}{\partial \tilde{a}^*_{1,N+1}}\right|_{\boldsymbol{e}^p} \cdot \left(\tilde{a}^*_{1,N+1} - \tilde{a}^p_{1,N+1}\right),\end{aligned} \tag{42}$$

where the vector $\boldsymbol{e}^p = (\bar{\lambda}^p_{c,N+1} \quad \tilde{\bar{a}}^p_{1,N+1})^T$ collects the predicted coupling variables at the macro-time point $\bar{T}_{N+1}$.

- Corrected coupling variables, which fulfill the coupling conditions at the macro-time point $\bar{T}_{N+1}$, can be derived by calculating the roots of the Eqs. (41) and (42)

$$\begin{aligned} &\bar{g}^B_{c\lambda,N+1}\left(\bar{\lambda}^*_{c,N+1}, \tilde{\bar{a}}^*_{1,N+1}\right) = 0 \\ &\bar{g}_{c\mu,N+1}\left(\bar{\lambda}^*_{c,N+1}, \tilde{\bar{a}}^*_{1,N+1}\right) = 0 \end{aligned} \quad \Longrightarrow \quad \bar{\lambda}_{c,N+1}, \tilde{\bar{a}}_{1,N+1}. \tag{43}$$

Step 3: Corrector Step

- Integrating subsystem 1 and subsystem 2 from $\bar{T}_N$ to $\bar{T}_{N+1}$ with the initial conditions (34a) and using an interpolation polynomial with the corrected coupling variables $\bar{\lambda}_{c,N+1}$ and $\tilde{\bar{a}}_{1,N+1}$ from Eq. (43), gives the corrected states and the corrected Lagrange multiplier

$$\bar{x}_{1,N+1}, \quad \bar{v}_{1,N+1} \quad \text{and} \quad \bar{x}_{2,N+1}, \quad \bar{v}_{2,N+1}, \quad \bar{\mu}_{2,N+1}. \tag{44}$$

Note that $\bar{x}_{1,N+1}$ and $\bar{v}_{1,N+1}$ are functions of $\bar{\lambda}_{c,N+1}, \bar{\lambda}_{c,N}, \ldots, \bar{\lambda}_{c,N-k+1}, \boldsymbol{z}_N$; $\bar{x}_{2,N+1}$, $\bar{v}_{2,N+1}$ and $\bar{\mu}_{2,N+1}$ depend on $\tilde{\bar{a}}_{1,N+1}, \tilde{\bar{a}}_{1,N}, \ldots, \tilde{\bar{a}}_{1,N-k+1}, \boldsymbol{z}_N$.

The corrected coupling variables of Eq. (43) are functions of the predicted states and accelerations and of the predicted coupling variables. In Eq. (43), the predicted acceleration variables can easily be eliminated with the help of the Eqs. (33a) and (33b), i.e. by means of

$$\begin{aligned} \bar{v}'^p_{1,N+1} &= -\bar{c}_1 \cdot \bar{x}^p_{1,N+1} - \bar{d}_1 \cdot \bar{v}^p_{1,N+1} + \bar{\lambda}^p_{c,N+1}, \\ \bar{v}'^p_{2,N+1} &= \tilde{\bar{a}}^p_{1,N+1}. \end{aligned} \tag{45}$$

Furthermore, the predicted position and velocity variables as well as the predicted Lagrange multiplier can be replaced with the help of Eq. (36) and the predicted coupling variables by means of Eq. (35) so that the corrected coupling variables $\bar{\lambda}_{c,N+1}$ and $\tilde{\bar{a}}_{1,N+1}$ of Eq. (43) can be expressed as functions of $\bar{\lambda}_{c,N}, \bar{\lambda}_{c,N-1}, \ldots, \bar{\lambda}_{c,N-k}, \tilde{\bar{a}}_{1,N}, \tilde{\bar{a}}_{1,N-1}, \ldots, \tilde{\bar{a}}_{1,N-k}, \boldsymbol{z}_N$. The final system of recurrence equations for the state variables, the Lagrange multiplier and the coupling variables has therefore the following structure

$$\begin{aligned} \bar{x}_{1,N+1} &= \bar{x}_{1,N+1}\left(\bar{\lambda}_{c,N+1}, \bar{\lambda}_{c,N}, \ldots, \bar{\lambda}_{c,N-k+1}, \boldsymbol{z}_N\right), \\ \bar{v}_{1,N+1} &= \bar{v}_{1,N+1}\left(\bar{\lambda}_{c,N+1}, \bar{\lambda}_{c,N}, \ldots, \bar{\lambda}_{c,N-k+1}, \boldsymbol{z}_N\right), \\ \bar{x}_{2,N+1} &= \bar{x}_{2,N+1}\left(\tilde{\bar{a}}_{1,N+1}, \tilde{\bar{a}}_{1,N}, \ldots, \tilde{\bar{a}}_{1,N-k+1}, \boldsymbol{z}_N\right), \\ \bar{v}_{2,N+1} &= \bar{v}_{2,N+1}\left(\tilde{\bar{a}}_{1,N+1}, \tilde{\bar{a}}_{1,N}, \ldots, \tilde{\bar{a}}_{1,N-k+1}, \boldsymbol{z}_N\right), \\ \bar{\mu}_{2,N+1} &= \bar{\mu}_{2,N+1}\left(\tilde{\bar{a}}_{1,N+1}, \tilde{\bar{a}}_{1,N}, \ldots, \tilde{\bar{a}}_{1,N-k+1}, \boldsymbol{z}_N\right), \\ \bar{\lambda}_{c,N+1} &= \bar{\lambda}_{c,N+1}\left(\bar{\lambda}_{c,N}, \bar{\lambda}_{c,N-1}, \ldots, \bar{\lambda}_{c,N-k}, \tilde{\bar{a}}_{1,N}, \tilde{\bar{a}}_{1,N-1}, \ldots, \tilde{\bar{a}}_{1,N-k}, \boldsymbol{z}_N\right), \\ \tilde{\bar{a}}_{1,N+1} &= \tilde{\bar{a}}_{1,N+1}\left(\bar{\lambda}_{c,N}, \bar{\lambda}_{c,N-1}, \ldots, \bar{\lambda}_{c,N-k}, \tilde{\bar{a}}_{1,N}, \tilde{\bar{a}}_{1,N-1}, \ldots, \tilde{\bar{a}}_{1,N-k}, \boldsymbol{z}_N\right). \end{aligned} \tag{46}$$

Eq. (46) represents 7 coupled linear recurrence equations of order $k+1$. The system only depends on the 5 parameters of the co-simulation test model.

2.2.2 Implicit co-simulation method based on weighted multiplier approach

Using the weighted multiplier approach, only step 2, in which the corrected coupling variables are calculated, has to be modified.

Step 1: Predictor Step

- Identical with step 1 in Sect. 2.2.1.

Step 2: Calculation of Corrected Coupling Variables

- Instead of using the coupling condition $\bar{g}^{B}_{c\lambda,N+1}(\bar{\lambda}^{*}_{c,N+1}, \tilde{\bar{a}}^{*}_{1,N+1})$ according to Eq. (41), we define the three coupling equations

$$\begin{aligned}\bar{g}^{pos}_{c\lambda,N+1}(\bar{\lambda}^{*}_{c,N+1}, \tilde{\bar{a}}^{*}_{1,N+1}) := \left(\bar{x}^{p}_{2,N+1} - \bar{x}^{p}_{1,N+1}\right) - \left.\frac{\partial \bar{x}^{*}_{1,N+1}}{\partial \bar{\lambda}^{*}_{c,N+1}}\right|_{\boldsymbol{e}^{p}} \cdot \left(\bar{\lambda}^{*}_{c,N+1} - \bar{\lambda}^{p}_{c,N+1}\right) \\ + \left.\frac{\partial \bar{x}^{*}_{2,N+1}}{\partial \tilde{\bar{a}}^{*}_{1,N+1}}\right|_{\boldsymbol{e}^{p}} \cdot \left(\tilde{\bar{a}}^{*}_{1,N+1} - \tilde{\bar{a}}^{p}_{1,N+1}\right), \end{aligned} \tag{47}$$

$$\begin{aligned}\bar{g}^{vel}_{c\lambda,N+1}(\bar{\lambda}^{*}_{c,N+1}, \tilde{\bar{a}}^{*}_{1,N+1}) := \left(\bar{v}^{p}_{2,N+1} - \bar{v}^{p}_{1,N+1}\right) - \left.\frac{\partial \bar{v}^{*}_{1,N+1}}{\partial \bar{\lambda}^{*}_{c,N+1}}\right|_{\boldsymbol{e}^{p}} \cdot \left(\bar{\lambda}^{*}_{c,N+1} - \bar{\lambda}^{p}_{c,N+1}\right) \\ + \left.\frac{\partial \bar{v}^{*}_{2,N+1}}{\partial \tilde{\bar{a}}^{*}_{1,N+1}}\right|_{\boldsymbol{e}^{p}} \cdot \left(\tilde{\bar{a}}^{*}_{1,N+1} - \tilde{\bar{a}}^{p}_{1,N+1}\right), \end{aligned} \tag{48}$$

$$\begin{aligned}\bar{g}^{acc}_{c\lambda,N+1}(\bar{\lambda}^{*}_{c,N+1}, \tilde{\bar{a}}^{*}_{1,N+1}) := \left(\bar{v}'^{p}_{2,N+1} - \bar{v}'^{p}_{1,N+1}\right) - \left.\frac{\partial \bar{v}'^{*}_{1,N+1}}{\partial \bar{\lambda}^{*}_{c,N+1}}\right|_{\boldsymbol{e}^{p}} \cdot \left(\bar{\lambda}^{*}_{c,N+1} - \bar{\lambda}^{p}_{c,N+1}\right) \\ + \left.\frac{\partial \bar{v}'^{*}_{2,N+1}}{\partial \tilde{\bar{a}}^{*}_{1,N+1}}\right|_{\boldsymbol{e}^{p}} \cdot \left(\tilde{\bar{a}}^{*}_{1,N+1} - \tilde{\bar{a}}^{p}_{1,N+1}\right). \end{aligned} \tag{49}$$

- The coupling condition $\bar{g}_{c\mu,N+1}$ of Eq. (42) remains unchanged.
- Combining Eq. (47) with Eq. (42) and solving this system for the coupling variables, yields

$$\begin{aligned}\bar{g}^{pos}_{c\lambda,N+1}\left(\bar{\lambda}^{pos}_{c,N+1}, \tilde{\bar{a}}^{pos}_{1,N+1}\right) = 0 \\ \bar{g}_{c\mu,N+1}\left(\bar{\lambda}^{pos}_{c,N+1}, \tilde{\bar{a}}^{pos}_{1,N+1}\right) = 0 \end{aligned} \quad \Longrightarrow \quad \bar{\lambda}^{pos}_{c,N+1}, \tilde{\bar{a}}^{pos}_{1,N+1}. \tag{50}$$

- Using Eq. (48) together with Eq. (42) and solving this system for the coupling variables, gives

$$\begin{aligned}\bar{g}^{vel}_{c\lambda,N+1}\left(\bar{\lambda}^{vel}_{c,N+1}, \tilde{\bar{a}}^{vel}_{1,N+1}\right) = 0 \\ \bar{g}_{c\mu,N+1}\left(\bar{\lambda}^{vel}_{c,N+1}, \tilde{\bar{a}}^{vel}_{1,N+1}\right) = 0 \end{aligned} \quad \Longrightarrow \quad \bar{\lambda}^{vel}_{c,N+1}, \tilde{\bar{a}}^{vel}_{1,N+1}. \tag{51}$$

- By combining Eq. (49) with Eq. (42) and solving this system for the coupling variables, one gets

$$\begin{aligned}\bar{g}^{acc}_{c\lambda,N+1}\left(\bar{\lambda}^{acc}_{c,N+1}, \tilde{\bar{a}}^{acc}_{1,N+1}\right) = 0 \\ \bar{g}_{c\mu,N+1}(\bar{\lambda}^{acc}_{c,N+1}, \tilde{\bar{a}}^{acc}_{1,N+1}) = 0 \end{aligned} \quad \Longrightarrow \quad \bar{\lambda}^{acc}_{c,N+1}, \tilde{\bar{a}}^{acc}_{1,N+1}. \tag{52}$$

- In the framework of the weighted multiplier approach, the corrected coupling variables are determined by

$$\begin{aligned}\bar{\lambda}_{c,N+1} &= \frac{1}{1+a+b} \cdot \left(\bar{\lambda}^{pos}_{c,N+1} + a \cdot \bar{\lambda}^{vel}_{c,N+1} + b \cdot \bar{\lambda}^{acc}_{c,N+1}\right), \\ \tilde{\bar{a}}_{1,N+1} &= \frac{1}{1+a+b} \cdot \left(\tilde{\bar{a}}^{pos}_{1,N+1} + a \cdot \tilde{\bar{a}}^{vel}_{1,N+1} + b \cdot \tilde{\bar{a}}^{acc}_{1,N+1}\right). \end{aligned} \tag{53}$$

Step 3: Corrector Step

- As step 3 in Sect. 2.2.1. However, instead of using the corrected coupling variables from Eq. (43), the corrected coupling variables from Eq. (53) are used.

Applying the weighted multiplier approach also yields a linear system of 7 coupled recurrence equations of order $k+1$. This system has the same structure as Eq. (46).

2.2.3 Implicit co-simulation method based on projection technique

Using the projection method in combination with a force/displacement-coupling approach, the following four steps have to be carried out.

Step 1: Predictor Step

- Identical with step 1 in Sect. 2.2.1.

Step 2: Calculation of Corrected Coupling Variables

- Identical with step 2 in Sect. 2.2.1 with one exception: Instead of calculating the corrected coupling variables according to Eq. (43), the corrected coupling variables $\bar{\lambda}_{c,N+1}^{acc}$ and $\tilde{\bar{a}}_{1,N+1}^{acc}$ of Eq. (52) are applied.

Step 3: Corrector Step

- As step 3 in Sect. 2.2.1, however $\bar{\lambda}_{c,N+1} = \bar{\lambda}_{c,N+1}^{acc}$ and $\tilde{\bar{a}}_{1,N+1} = \tilde{\bar{a}}_{1,N+1}^{acc}$ are used as corrected coupling variables. Result of the subsystem integration are the corrected state variables and the corrected Lagrange multiplier

$$\bar{x}_{1,N+1}, \quad \bar{v}_{1,N+1} \quad \text{and} \quad \bar{x}_{2,N+1}, \quad \bar{v}_{2,N+1}, \quad \bar{\mu}_{2,N+1}. \tag{54}$$

  Note that $\bar{x}_{1,N+1}$ and $\bar{v}_{1,N+1}$ are depending on $\bar{\lambda}_{c,N+1}, \bar{\lambda}_{c,N}, \ldots, \bar{\lambda}_{c,N-k+1}, \boldsymbol{z}_N$, while $\bar{x}_{2,N+1}$, $\bar{v}_{2,N+1}$ and $\bar{\mu}_{2,N+1}$ are functions of $\tilde{\bar{a}}_{1,N+1}, \tilde{\bar{a}}_{1,N}, \ldots, \tilde{\bar{a}}_{1,N-k+1}, \boldsymbol{z}_N$.
- The corrected coupling variables $\bar{\lambda}_{c,N+1} = \bar{\lambda}_{c,N+1}^{acc}$ and $\tilde{\bar{a}}_{1,N+1} = \tilde{\bar{a}}_{1,N+1}^{acc}$ according to Eq. (52) are functions of the predicted accelerations, the predicted Lagrange multiplier and of the predicted coupling variables. By eliminating the predicted variables with the help of Eq. (35), Eq. (36) and Eq. (45), the corrected coupling variables $\bar{\lambda}_{c,N+1}$ and $\tilde{\bar{a}}_{1,N+1}$ can finally be expressed as functions of $\bar{\lambda}_{c,N}, \bar{\lambda}_{c,N-1}, \ldots, \bar{\lambda}_{c,N-k}, \tilde{\bar{a}}_{1,N}, \tilde{\bar{a}}_{1,N-1}, \ldots, \tilde{\bar{a}}_{1,N-k}, \boldsymbol{z}_N$.

Step 4: Projection Step

- Projected position and velocity variables are calculated by

$$\bar{x}_{N+1} = \frac{\bar{x}_{1,N+1} + \alpha_{m21} \cdot \bar{x}_{2,N+1}}{1 + \alpha_{m21}}, \quad \bar{v}_{N+1} = \frac{\bar{v}_{1,N+1} + \alpha_{m21} \cdot \bar{v}_{2,N+1}}{1 + \alpha_{m21}}. \tag{55}$$

Eq. (55) together with the corrected coupling variables $\bar{\lambda}_{c,N+1}, \tilde{\bar{a}}_{1,N+1}$ and the Lagrange multiplier $\bar{\mu}_{2,N+1}$ from Eq. (54) represent a system of five coupled linear recurrence equations of order $k+1$. Note that the vector $\boldsymbol{z}_N$ contains the initial conditions for the macro-time step $\bar{T}_N \to \bar{T}_{N+1}$. Due to the fact that a projection step has also been accomplished at the macro-time point $\bar{T}_N$, we can conclude that $\boldsymbol{z}_N = (\bar{x}_{1,N}, \bar{v}_{1,N}, \bar{x}_{2,N}, \bar{v}_{2,N})^T = (\bar{x}_N, \bar{v}_N, \bar{x}_N, \bar{v}_N)^T$. Consequently, the governing recurrence system consisting of 5 linear equations of order $k+1$ is structurally given by

$$\begin{aligned}
\bar{x}_{N+1} &= \bar{x}_{N+1}\left(\bar{\lambda}_{c,N+1}, \bar{\lambda}_{c,N}, \ldots, \bar{\lambda}_{c,N-k+1}, \tilde{\bar{a}}_{1,N+1}, \tilde{\bar{a}}_{1,N}, \ldots, \tilde{\bar{a}}_{1,N-k+1}, \bar{x}_N, \bar{v}_N\right), \\
\bar{v}_{N+1} &= \bar{v}_{N+1}\left(\bar{\lambda}_{c,N+1}, \bar{\lambda}_{c,N}, \ldots, \bar{\lambda}_{c,N-k+1}, \tilde{\bar{a}}_{1,N+1}, \tilde{\bar{a}}_{1,N}, \ldots, \tilde{\bar{a}}_{1,N-k+1}, \bar{x}_N, \bar{v}_N\right), \\
\bar{\mu}_{2,N+1} &= \bar{\mu}_{2,N+1}\left(\tilde{\bar{a}}_{1,N+1}, \tilde{\bar{a}}_{1,N}, \ldots, \tilde{\bar{a}}_{1,N-k+1}, \bar{x}_N, \bar{v}_N\right), \\
\bar{\lambda}_{c,N+1} &= \bar{\lambda}_{c,N+1}\left(\bar{\lambda}_{c,N}, \bar{\lambda}_{c,N-1}, \ldots, \bar{\lambda}_{c,N-k}, \tilde{\bar{a}}_{1,N}, \tilde{\bar{a}}_{1,N-1}, \ldots, \tilde{\bar{a}}_{1,N-k}, \bar{x}_N, \bar{v}_N\right), \\
\tilde{\bar{a}}_{1,N+1} &= \tilde{\bar{a}}_{1,N+1}\left(\bar{\lambda}_{c,N}, \bar{\lambda}_{c,N-1}, \ldots, \bar{\lambda}_{c,N-k}, \tilde{\bar{a}}_{1,N}, \tilde{\bar{a}}_{1,N-1}, \ldots, \tilde{\bar{a}}_{1,N-k}, \bar{x}_N, \bar{v}_N\right).
\end{aligned} \tag{56}$$

2.3 Displacement/Displacement-coupling

In connection with a displacement/displacement-decomposition approach, application of the Baumgarte and of the weighted multiplier method is not treated here. Only the projection method is discussed in the following.

2.3.1 Implicit co-simulation method based on projection technique

Applying a displacement/displacement-coupling approach, the two-mass oscillator is decomposed into two subsystems so that both subsystems are kinematically driven single-mass oscillators, see Fig. 4. The kinematical motions are applied

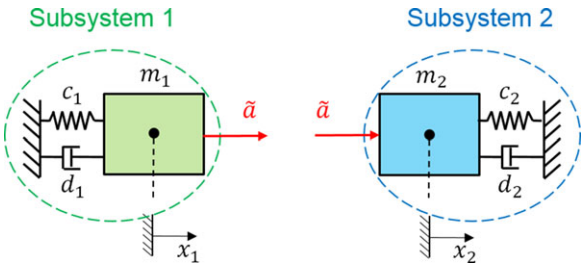

Fig. 4 Co-simulation test model: displacement/displacement-decomposition approach.

on acceleration (index-1) level, i.e. the accelerations of mass m_1 and mass m_2 are prescribed by rheonomic constraint equations. Due to the fact that both masses are coupled by a rigid link, accelerations of m_1 and m_2 are equal and in the following denoted by $\tilde{\bar{a}}(t)$. Prescribing the acceleration $\tilde{\bar{a}}(t)$ in subsystem 1 is accomplished by the rheonomic constraint equation $\bar{v}_1' - \tilde{\bar{a}} = 0$ and the corresponding Lagrange multiplier $\bar{\mu}_1$. Accordingly, applying the motion $\tilde{\bar{a}}(t)$ in subsystem 2 is realized by the rheonomic constraint equation $\bar{v}_2' - \tilde{\bar{a}} = 0$ and the corresponding Lagrange multiplier $\bar{\mu}_2$. Since the two masses are coupled by a rigid link, the coupling forces $\bar{\mu}_1$ and $\bar{\mu}_2$ must be equal. Hence, the coupling condition simply reads $\bar{g}_{c\mu} := \bar{\mu}_2 - \bar{\mu}_1 = 0$.

The DAE system characterizing the decomposed system is given by

Subsystem 1:

$$\bar{x}_1' = \bar{v}_1, \quad \bar{v}_1' = -\bar{c}_1 \cdot \bar{x}_1 - \bar{d}_1 \cdot \bar{v}_1 + \bar{\mu}_1, \quad \bar{v}_1' - \tilde{\bar{a}} = 0, \tag{57a}$$

Subsystem 2:

$$\bar{x}_2' = \bar{v}_2, \quad \bar{v}_2' = -\frac{\alpha_{c21}}{\alpha_{m21}} \cdot \bar{c}_1 \cdot \bar{x}_2 - \frac{\alpha_{d21}}{\alpha_{m21}} \cdot \bar{d}_1 \cdot \bar{v}_2 - \frac{1}{\alpha_{m21}} \cdot \bar{\mu}_2, \quad \bar{v}_2' - \tilde{\bar{a}} = 0, \tag{57b}$$

Coupling condition:

$$\bar{g}_{c\mu} := \bar{\mu}_2 - \bar{\mu}_1 = 0. \tag{57c}$$

In order to derive the governing system of recurrence equations, we again analyze the general macro-time step from $\bar{T}_N$ to $\bar{T}_{N+1}$. At the beginning of the macro-step, the state variables, the Lagrange multipliers and the coupling variable are given by

$$\begin{aligned} \bar{x}_1(\bar{T}_N) &= \bar{x}_{1,N}, & \bar{v}_1(\bar{T}_N) &= \bar{v}_{1,N}, \\ \bar{x}_2(\bar{T}_N) &= \bar{x}_{2,N}, & \bar{v}_2(\bar{T}_N) &= \bar{v}_{2,N}, \\ \bar{\mu}_1(\bar{T}_N) &= \bar{\mu}_{1,N}, & \bar{\mu}_2(\bar{T}_N) &= \bar{\mu}_{2,N}, \end{aligned} \tag{58a}$$

$$\tilde{\bar{a}}(\bar{T}_N) = \tilde{\bar{a}}_N. \tag{58b}$$

Step 1: Predictor Step

- With the initial conditions (58a) and the predictor (extrapolation) polynomial

$$\tilde{\bar{a}}^p(\bar{t}) = P_{\tilde{\bar{a}}}^p \left[\left(\bar{T}_N, \tilde{\bar{a}}_N\right), \left(\bar{T}_{N-1}, \tilde{\bar{a}}_{N-1}\right), \ldots, \left(\bar{T}_{N-k}, \tilde{\bar{a}}_{N-k}\right); \bar{t} \right], \tag{59}$$

an analytical integration of the two subsystems from $\bar{T}_N$ to $\bar{T}_{N+1}$ yields the predicted state variables and the predicted Lagrange multipliers at the macro-time point $\bar{T}_{N+1}$, i.e.

$$\bar{x}_{1,N+1}^p, \quad \bar{v}_{1,N+1}^p, \quad \bar{\mu}_{1,N+1}^p \quad \text{and} \quad \bar{x}_{2,N+1}^p, \quad \bar{v}_{2,N+1}^p, \quad \bar{\mu}_{2,N+1}^p, \tag{60}$$

which are functions of $\tilde{\bar{a}}_N, \tilde{\bar{a}}_{N-1}, \ldots, \tilde{\bar{a}}_{N-k}, \boldsymbol{z}_N$.

Step 2: Calculation of Corrected Coupling Variable

- Making use of the interpolation polynomial

$$\tilde{\bar{a}}^*(\bar{t}) = P^*_{\tilde{\bar{a}}}\left[\left(\bar{T}_{N+1}, \tilde{\bar{a}}^*_{N+1}\right), \left(\bar{T}_N, \tilde{\bar{a}}_N\right), \ldots, \left(\bar{T}_{N-k+1}, \tilde{\bar{a}}_{N-k+1}\right); \bar{t}\right], \tag{61}$$

an integration from $\bar{T}_N$ to $\bar{T}_{N+1}$ with initial conditions (58a) gives the state variables and Lagrange multipliers

$$\bar{x}^*_{1,N+1}, \quad \bar{v}^*_{1,N+1}, \quad \bar{\mu}^*_{1,N+1} \quad \text{and} \quad \bar{x}^*_{2,N+1}, \quad \bar{v}^*_{2,N+1}, \quad \bar{\mu}^*_{2,N+1} \tag{62}$$

at the macro-time point $\bar{T}_{N+1}$, which are depending on $\tilde{\bar{a}}^*_{N+1}, \tilde{\bar{a}}_N, \ldots, \tilde{\bar{a}}_{N-k+1}, z_N$.
- Differentiation with respect to $\tilde{\bar{a}}^*_{N+1}$, which denotes an arbitrary coupling variable at $\bar{T}_{N+1}$, yields

$$\begin{aligned}
\frac{\partial \bar{x}^*_{1,N+1}}{\partial \tilde{\bar{a}}^*_{N+1}} &= const., \quad \frac{\partial \bar{v}^*_{1,N+1}}{\partial \tilde{\bar{a}}^*_{N+1}} = const., \\
\frac{\partial \bar{x}^*_{2,N+1}}{\partial \tilde{\bar{a}}^*_{N+1}} &= const., \quad \frac{\partial \bar{v}^*_{2,N+1}}{\partial \tilde{\bar{a}}^*_{N+1}} = const., \\
\frac{\partial \bar{\mu}^*_{1,N+1}}{\partial \tilde{\bar{a}}^*_{N+1}} &= const., \quad \frac{\partial \bar{\mu}^*_{2,N+1}}{\partial \tilde{\bar{a}}^*_{N+1}} = const..
\end{aligned} \tag{63}$$

- At the fixed macro-time point $\bar{T}_{N+1}$, the coupling condition $\bar{g}_{c\mu,N+1}$ is regarded as a function of the general coupling variable $\tilde{\bar{a}}^*_{N+1}$

$$\bar{g}_{c\mu,N+1}\left(\tilde{\bar{a}}^*_{N+1}\right) := \bar{\mu}^*_{2,N+1}\left(\tilde{\bar{a}}^*_{N+1}\right) - \bar{\mu}^*_{1,N+1}\left(\tilde{\bar{a}}^*_{N+1}\right). \tag{64}$$

Due to the linearity of the problem, the coupling condition can be rewritten as

$$\begin{aligned}
\bar{g}_{c\mu,N+1}(\tilde{\bar{a}}^*_{N+1}) &:= \bar{g}_{c\mu,N+1}(\tilde{\bar{a}}^p_{N+1}) + \left.\frac{\partial \bar{g}_{c\mu,N+1}}{\partial \tilde{\bar{a}}^*_{N+1}}\right|_{\tilde{\bar{a}}^p_{N+1}} \cdot (\tilde{\bar{a}}^*_{N+1} - \tilde{\bar{a}}^p_{N+1}) \\
&= \bar{\mu}^p_{2,N+1} - \bar{\mu}^p_{1,N+1} + \left(\left.\frac{\partial \bar{\mu}^*_{2,N+1}}{\partial \tilde{\bar{a}}^*_{N+1}}\right|_{\tilde{\bar{a}}^p_{N+1}} - \left.\frac{\partial \bar{\mu}^*_{1,N+1}}{\partial \tilde{\bar{a}}^*_{N+1}}\right|_{\tilde{\bar{a}}^p_{N+1}} \right) \cdot (\tilde{\bar{a}}^*_{N+1} - \tilde{\bar{a}}^p_{N+1}).
\end{aligned} \tag{65}$$

- A corrected coupling variable, which enforces the coupling condition at the macro-time point $\bar{T}_{N+1}$, can be obtained by setting Eq. (65) equal to zero and by solving this equation for the coupling variable. One obtains

$$\tilde{\bar{a}}_{N+1} = \tilde{\bar{a}}^p_{N+1} - \frac{\bar{\mu}^p_{2,N+1} - \bar{\mu}^p_{1,N+1}}{\left.\frac{\partial \bar{\mu}^*_{2,N+1}}{\partial \tilde{\bar{a}}^*_{N+1}}\right|_{\tilde{\bar{a}}^p_{N+1}} - \left.\frac{\partial \bar{\mu}^*_{1,N+1}}{\partial \tilde{\bar{a}}^*_{N+1}}\right|_{\tilde{\bar{a}}^p_{N+1}}}. \tag{66}$$

Step 3: Corrector Step

- Using the corrected coupling variable $\tilde{\bar{a}}_{N+1}$ from Eq. (66), subsystem integration from $\bar{T}_N$ to $\bar{T}_{N+1}$ with initial conditions (58a) yields the corrected states and Lagrange multipliers

$$\bar{x}_{1,N+1}, \quad \bar{v}_{1,N+1}, \quad \bar{\mu}_{1,N+1} \quad \text{and} \quad \bar{x}_{2,N+1}, \quad \bar{v}_{2,N+1}, \quad \bar{\mu}_{2,N+1}, \tag{67}$$

which are functions of $\tilde{\bar{a}}_{N+1}, \tilde{\bar{a}}_N, \ldots, \tilde{\bar{a}}_{N-k+1}, z_N$.

Step 4: Projection Step

- Projected position and velocity variables are calculated by

$$\bar{x}_{N+1} = \frac{\bar{x}_{1,N+1} + \alpha_{m21} \cdot \bar{x}_{2,N+1}}{1 + \alpha_{m21}}, \quad \bar{v}_{N+1} = \frac{\bar{v}_{1,N+1} + \alpha_{m21} \cdot \bar{v}_{2,N+1}}{1 + \alpha_{m21}}. \tag{68}$$

In Eq. (66), the predicted variables can be replaced with the help of Eqs. (59) and (60). This results in a relationship of the form

$$\tilde{\bar{a}}_{N+1} = \tilde{\bar{a}}_{N+1}\left(\tilde{\bar{a}}_N, \tilde{\bar{a}}_{N-1}, \ldots, \tilde{\bar{a}}_{N-k}, z_N\right). \tag{69}$$

Thus, the governing recurrence system consisting of 5 linear equations of order $k+1$ for the projected state variables, the Lagrange multipliers and the coupling variable can finally be expressed as

$$\begin{aligned}
\bar{x}_{N+1} &= \bar{x}_{N+1}\left(\tilde{\bar{a}}_{N+1}, \tilde{\bar{a}}_N, \ldots, \tilde{\bar{a}}_{N-k+1}, \bar{x}_N, \bar{v}_N\right), \\
\bar{v}_{N+1} &= \bar{v}_{N+1}\left(\tilde{\bar{a}}_{N+1}, \tilde{\bar{a}}_N, \ldots, \tilde{\bar{a}}_{N-k+1}, \bar{x}_N, \bar{v}_N\right), \\
\bar{\mu}_{1,N+1} &= \bar{\mu}_{1,N+1}\left(\tilde{\bar{a}}_{N+1}, \tilde{\bar{a}}_N, \ldots, \tilde{\bar{a}}_{N-k+1}, \bar{x}_N, \bar{v}_N\right), \\
\bar{\mu}_{2,N+1} &= \bar{\mu}_{2,N+1}\left(\tilde{\bar{a}}_{N+1}, \tilde{\bar{a}}_N, \ldots, \tilde{\bar{a}}_{N-k+1}, \bar{x}_N, \bar{v}_N\right), \\
\tilde{\bar{a}}_{N+1} &= \tilde{\bar{a}}_{N+1}\left(\tilde{\bar{a}}_N, \tilde{\bar{a}}_{N-1}, \ldots, \tilde{\bar{a}}_{N-k}, \bar{x}_N, \bar{v}_N\right).
\end{aligned} \tag{70}$$

Remark: For the linear co-simulation test model and in case of an analytical subsystem integration, the predicted and the corrected position and velocity variables of both subsystems are equal ($\bar{x}^p_{1,N+1} = \bar{x}^p_{2,N+1}$, $\bar{v}^p_{1,N+1} = \bar{v}^p_{2,N+1}$, $\bar{x}_{1,N+1} = \bar{x}_{2,N+1}$ and $\bar{v}_{1,N+1} = \bar{v}_{2,N+1}$), i.e. there is no drift-off effect. Thus, the projection step 4 is not necessary if displacement/displacement-decomposition is applied. In our representation, the projection step has been described in order to show the general procedure of the projection method in connection with a displacement/displacement-decomposition approach. For nonlinear problems or in case of a numerical subsystem integration, the projection step is required in order to avoid the drift-off effect.

Using the Baumgarte approach in connection with displacement/displacement-decomposition, the rheonomic constraint equations $\bar{v}_1' - \tilde{\bar{a}} = 0$ and $\bar{v}_2' - \tilde{\bar{a}} = 0$ in Eq. (57a) and Eq. (57b) have to be replaced by the Baumgarte functions $0 = (\bar{x}_1 - \tilde{\bar{x}}) + \bar{\beta}\cdot(\bar{v}_1 - \tilde{\bar{v}}) + \bar{\gamma}\cdot(\bar{v}_1' - \tilde{\bar{a}})$ and $0 = (\bar{x}_2 - \tilde{\bar{x}}) + \bar{\beta}\cdot(\bar{v}_2 - \tilde{\bar{v}}) + \bar{\gamma}\cdot(\bar{v}_2' - \tilde{\bar{a}})$, where $\tilde{\bar{x}}$, $\tilde{\bar{v}} = \frac{d}{d\bar{t}}\tilde{\bar{x}}$ and $\tilde{\bar{a}} = \frac{d}{d\bar{t}}\tilde{\bar{v}}$ represent the applied kinematical motion on position, velocity and acceleration level. Since motion has also to be applied on position level, $\tilde{\bar{x}}(\bar{t})$ has to be at least a quadratic function with respect to time $\bar{t}$ in order to obtain continuous state variables at the macro-time points. Since constant and linear approximation polynomials cannot be used, the Baumgarte and the weighted multiplier method are not discussed here in context with displacement/displacement-decomposition.

3 Results: Stability and convergence plots for the three implicit co-simulation methods

The numerical stability of the co-simulation test model depends on 5 independent parameters. Instead of using the 5 parameters defined in Eq. 5, it might be more useful to choose 5 other parameters. Bearing in mind the stability definition for numerical time integration schemes, where the two parameters $h\lambda_r$ and $h\lambda_i$ are used to characterize the stability behavior, employing the following 5 independent parameters for the co-simulation test model might be more convenient

$$\begin{aligned}
&\bar{\lambda}_{r1} = -\frac{\bar{d}_1}{2}, \quad \bar{\lambda}_{i1} = \frac{1}{2}\sqrt{4\cdot\bar{c}_1 - \bar{d}_1^2}, \\
&\alpha_{m21} = \frac{m_2}{m_1}, \quad \alpha_{\lambda r21} = \frac{\bar{\lambda}_{r2}}{\bar{\lambda}_{r1}} = \frac{\alpha_{d21}}{\alpha_{m21}}, \quad \alpha_{\lambda i21} = \frac{\bar{\lambda}_{i2}}{\bar{\lambda}_{i1}} = \frac{1}{\alpha_{m21}}\frac{\sqrt{4\cdot\alpha_{m21}\cdot\alpha_{c21}\cdot\bar{c}_1 - \alpha_{d21}^2\cdot\bar{d}_1^2}}{\sqrt{4\cdot\bar{c}_1 - \bar{d}_1^2}}.
\end{aligned} \tag{71}$$

The 5 parameters defined in Eq. (71) are easily explained. $\bar{\lambda}_{r1}$ and $\bar{\lambda}_{i1}$ characterize subsystem 1 and denote the real and imaginary part of the eigenvalue of subsystem 1. α_{m21} terms the mass ratio. The two parameters $\bar{\alpha}_{\lambda r21}$ and $\bar{\alpha}_{\lambda i21}$ specify subsystem 2 and describe the damping and the frequency ratio. The stability of a co-simulation approach, i.e. the spectral radius of the corresponding system of recurrence equations, is uniquely defined by the 5 independent parameters of Eq. (71). Thus, fixing three parameters, the spectral radius can be plotted as a function of the remaining two parameters in 2D stability plots according to the well-established 2D stability plots for time integration schemes.

In the following sections, the three parameters α_{m21}, $\alpha_{\lambda r21}$ and $\alpha_{\lambda i21}$ are fixed and 2D stability plots are presented as a function of $\bar{\lambda}_{r1}$ and $\bar{\lambda}_{i1}$. Therefore, the parameters $\bar{\lambda}_{r1}$ and $\bar{\lambda}_{i1}$ are varied in the range $[-2, 0]$ and $[0, 2]$. Specifying the 5 parameters of the co-simulation test model, the spectral radius ρ of the governing system of recurrence equations can be calculated numerically. In the plots, stable parameter configurations are indicated by a green circle, i.e. points for which $\rho \leq 1$ holds. To reduce floating point errors, calculation of ρ has been carried out with 128 decimal places.

For the reason of a clear representation, all stability plots are collected in the Appendix. The discussion of the plots is carried out in the subsequent sections.

3.1 Stability plots: Force/Force-coupling (Index-1)

3.1.1 Implicit co-simulation method based on baumgarte stabilization ($\bar{\mu} = 1$)

Stability plots for the implicit co-simulation method based on the Baumgarte stabilization technique are collected in Fig. 9 in Appendix A (see Wiley online library, also the following Figs.). Applying the Baumgarte method, the two parameters $\bar{\beta}$ and $\bar{\gamma}$ have to be specified, see Eq. (7c). In literature, the two Baumgarte parameters are frequently replaced by one single parameter $\bar{\mu}$ by setting $\bar{\beta} = 2\bar{\mu}$ and $\bar{\gamma} = \bar{\mu}^2$. The plots in Fig. 9 were generated with $\bar{\mu} = 1$. In the left column, stability plots are collected for the case of constant approximation ($k = 0$) for the four parameter sets ($\alpha_{m21} = 1$, $\alpha_{\lambda r21} = 1$, $\alpha_{\lambda i21} = 1$), ($\alpha_{m21} = 10$, $\alpha_{\lambda r21} = 1$, $\alpha_{\lambda i21} = 1$), ($\alpha_{m21} = 1$, $\alpha_{\lambda r21} = 10$, $\alpha_{\lambda i21} = 1$) and ($\alpha_{m21} = 1$, $\alpha_{\lambda r21} = 1$, $\alpha_{\lambda i21} = 10$). The column in the middle contains the plots for the case that linear approximation polynomials are used ($k = 1$). The corresponding plots for quadratic approximation polynomials ($k = 2$) are arranged in the right column. As can be detected, stable simulations are obtained in a wide range of the parameters $\bar{\lambda}_{r1}$ and $\bar{\lambda}_{i1}$ for constant, linear and quadratic approximation polynomials. The influence of the mass ratio coefficient α_{m21} and the damping ratio coefficient $\alpha_{\lambda r21}$ on the stability behavior is marginal. As can be seen in the fourth row, the crucial parameter for the stability is the frequency ratio coefficient $\alpha_{\lambda i21}$. For $k = 0$, the region of stability is significantly reduced. For $k = 1$ and $k = 2$, most of the points remain stable (the zoom in the lower right plot indicates that the method is stable for $\bar{\lambda}_{r1}, \bar{\lambda}_{i1} \to 0$).

3.1.2 Implicit co-simulation method based on weighted multiplier approach ($a = b = 1$)

Fig. 10 collects the corresponding plots for the weighted multiplier approach. The plots have been generated with the parameters $a = b = 1$. Compared with the Baumgarte method, we observe a reduced stability for $k = 0$. For $k = 1$, the weighted multiplier approach shows almost the same stability behavior as the Baumgarte approach. For $k = 2$, however, the weighted multiplier approach shows an unstable region close the vertical axes as can be seen in the zoom plots. Hence, for $a = b = 1$ and for the case that quadratic approximation polynomials are used, the weighted multiplier method is not stable for $\bar{\lambda}_{r1}, \bar{\lambda}_{i1} \to 0$.

3.1.3 Implicit co-simulation method based on projection technique

Results for the projection method are arranged in Fig. 11. The plots indicate that the region of stability will notably be reduced if the damping ratio parameter $\alpha_{\lambda r21}$ or the frequency ratio parameter $\alpha_{\lambda i21}$ is increased.

3.2 Stability plots: Force/Displacement-coupling (Index-1)

3.2.1 Implicit co-simulation method based on baumgarte stabilization ($\bar{\mu} = 1$)

Stability plots for the co-simulation method based on Baumgarte stabilization in connection with force/displacement-decomposition are collected in Fig. 12 in Appendix B (see Wiley online library). Compared with the results in Sect. 3.1.1, one observes an improved stability behavior for $k = 0$. For $k = 1$ and $k = 2$, however, force/force-decomposition is more stable.

3.2.2 Implicit co-simulation method based on weighted multiplier approach ($a = b = 1$)

Applying a force/displacement-decomposition technique in combination with the weighted multiplier approach yields the stability plots depicted in Fig. 13. Compared with the corresponding plots in Sect. 3.1.2, it can be noticed that the force/displacement-decomposition approach shows an improved stability behavior for $k = 0$. For $k = 1$ and $k = 2$, force/force-decomposition yields better results.

3.2.3 Implicit co-simulation method based on projection technique

Using the projection method in combination with a force/displacement-decomposition approach gives the stability plots collected in Fig. 14. The stability plots are similar to the corresponding plots in Sect. 3.1.3 for the force/force-decomposition approach.

It should finally be stressed that a force/displacement-decomposition approach (subsystem 1 is a force-driven and subsystem 2 a base-point excited single-mass oscillator, see Sect. 2.2) may show a different stability behavior as a displacement/force-decomposition approach (subsystem 1 is a base-point excited and subsystem 2 a force-driven single-mass oscillator) due to the asymmetry introduced by this decomposition technique.

3.3 Stability plots: Displacement/Displacement-coupling

3.3.1 Implicit co-simulation method based on projection technique

Fig. 15 in Appendix C (see Wiley online library) depicts stability plots for the co-simulation method based on the projection technique for the case that a displacement/displacement-decomposition approach is applied. Compared with the results in Sect. 3.1.3 (force/force-decomposition) and Sect. 3.2.3 (force/displacement-decomposition), it can be observed that displacement/displacement-decomposition shows the best stability behavior. For $k = 0$, we only detect stable points.

3.4 Stability plots: Force/Force-coupling (Index-2)

3.4.1 Implicit co-simulation method based on baumgarte stabilization

Setting the Baumgarte parameters $\bar{\beta} = 2\bar{\mu}$ and $\bar{\gamma} = 0$ yields a co-simulation approach on index-2 level. Stability plots for $\bar{\mu} = 0.25$, $\bar{\mu} = 1$ and $\bar{\mu} = 5$ are collected in Fig. 16 in Appendix D (see Wiley online library) for constant $(k = 0)$, linear $(k = 1)$ and quadratic $(k = 2)$ approximation polynomials. For the reason of a concise representation, we only present stability plots for $\alpha_{m21} = 2$, $\alpha_{\lambda r21} = 2$, $\alpha_{\lambda i21} = 2$ in connection with a force/force-decomposition approach. For $k = 0$, the index-2 approach shows a good stability behavior. The plots exhibit that the influence of $\bar{\mu}$ on the stability behavior is small. Further simulations, which are not shown here, indicate that choosing smaller Baumgarte parameters may (slightly) improve the stability. For $k = 1$ and $k = 2$, the index-2 approach exhibits a bad performance (loss of stability for $\bar{\lambda}_{r1}, \bar{\lambda}_{i1} \to 0$) and may practically only be applied for larger values of $\bar{\mu}$ with the drawback of a reduced accuracy.

3.4.2 Implicit co-simulation method based on weighted multiplier approach

For $a > 0$ and $b = 0$, an index-2 approach is obtained. Fig. 17 contains stability plots for $a = 0.5, a = 1$ and $a = 5$ for the case of constant $(k = 0)$, linear $(k = 1)$ and quadratic $(k = 2)$ approximation. The plots have been generated with the parameters $\alpha_{m21} = 2$, $\alpha_{\lambda r21} = 2$, $\alpha_{\lambda i21} = 2$ using a force/force-decomposition approach. Good stability behavior is observed for $k = 0$. Additional simulations, which are not presented here, indicate that the stability for $k = 0$ may (slightly) be increased by choosing smaller values for the parameter a. A reduced stability behavior is detected for $k = 1$ and $k = 2$. Using linear and quadratic approximation, the parameter a has to be increased in order to obtain stable results, which however reduces the accuracy of the method so that – from the practical point of view – the cases $k = 1$ and $k = 2$ may only be of minor interest.

3.5 Stability plots: Force/Force-coupling (Index-3)

For $\bar{\beta} = \bar{\gamma} = 0$ and $a = b = 0$ the Baumgarte and the weighted multiplier method are identical and we obtain an index-3 approach. Results for the index-3 formulation with $\alpha_{m21} = 2$, $\alpha_{\lambda r21} = 2$, $\alpha_{\lambda i21} = 2$ based on a force/force-decomposition approach are arranged in Fig. 18 in Appendix E (see Wiley online library). Using constant approximation $(k = 0)$, a good stability behavior is achieved, whereas only unstable points are observed for linear and quadratic approximation.

Remark: Although the index-3 approach may yield stable results, it should be mentioned that artifical oscillations (chattering) are observed in the Lagrange multiplier, see, for instance, Ref. [34]. The frequency of this artifical oscillation is related to the macro-step size H; its amplitude decreases if H is reduced.

3.6 Influence of the baumgarte and the weighted multiplier parameters on the stability behavior (Index-1)

3.6.1 Implicit co-simulation method based on baumgarte stabilization

To illustrate the influence of the Baumgarte parameter $\bar{\mu}$ on the stability behavior, we consider an index-1 co-simulation approach based on force/force-decomposition with $\alpha_{m21} = 2, \alpha_{\lambda r21} = 2, \alpha_{\lambda i21} = 2$. Fig. 19 in Appendix F (see Wiley online library) depicts stability plots for $\bar{\mu} = 0.25$, $\bar{\mu} = 1$ and $\bar{\mu} = 5$. As can be seen, for $k = 0$ the stability can be improved by reducing $\bar{\mu}$. For $k = 1$ and $k = 2$, increasing the parameter $\bar{\mu}$ improves the stability behavior.

3.6.2 Implicit co-simulation method based on weighted multiplier approach

The influence of the parameters a and b on the stability behavior of the weighted multiplier approach with force/force-decomposition is illustrated in Fig. 20. The plots have been generated with $\alpha_{m21} = 2, \alpha_{\lambda r21} = 2, \alpha_{\lambda i21} = 2$. Using constant

approximation, the stability may be increased by using smaller values for a and b. In contrast, for $k = 1$ and $k = 2$ the stability can be increased by using larger values for a and b.

3.7 Convergence plots: Force/Force-coupling (Index-1, Index-2 and Index-3)

In order to compare the three co-simulation approaches, besides the numerical stability there are also the convergence behavior and the numerical error of interest. Therefore, convergence plots have been generated using the co-simulation test model with the following parameters: $m_1 = 1$, $m_2 = 2$, $c_1 = c_2 = 1000$, $d_1 = d_2 = 10$. In this work, the relative global error ε_{glo} for the position and velocity variables is computed by the normalized root mean square error (NRMSE) according to

$$\varepsilon_{glo} = \left[\frac{\sum_N (x_1(T_N) - x_{1,N})^2}{\sum_N (x_1(T_N) - x_{1,mean})^2} + \frac{\sum_N (x_2(T_N) - x_{2,N})^2}{\sum_N (x_2(T_N) - x_{2,mean})^2} \right. \\ \left. \frac{\sum_N (v_1(T_N) - v_{1,N})^2}{\sum_N (v_1(T_N) - v_{1,mean})^2} + \frac{\sum_N (v_2(T_N) - v_{2,N})^2}{\sum_N (v_2(T_N) - v_{2,mean})^2} \right]^{1/2} \tag{72}$$

$$\text{with} \quad x_{1,mean} = \sum_N \frac{x_1(T_N)}{N_{total}}, \quad x_{2,mean} = \sum_N \frac{x_2(T_N)}{N_{total}},$$

$$v_{1,mean} = \sum_N \frac{v_1(T_N)}{N_{total}}, \quad v_{2,mean} = \sum_N \frac{v_2(T_N)}{N_{total}}.$$

In the above equation, the values $x_{1,N}$,$x_{2,N}$ and $v_{1,N}$,$v_{2,N}$ denote the co-simulation results (the solution of the system of recurrence equations). $x_1(T_N)$, $x_2(T_N)$ and $v_1(T_N)$, $v_2(T_N)$ term the values of the analytical solution at the macro-time point T_N. The total number of macro-steps is indicated by N_{total}. The NRMSE is defined by the mean value of the squared difference between the reference and the numerical solution devided by the variance of the reference solution. Instead of using the variance in the denominator, the mean value $x^2_{1,mean}$ could also be used. Application of the NRMSE is, however, more appropriate for time series, where the mean value might become zero or close to zero. The solution of the co-simulation test model is an exponentially decaying oscillation (at least for small damping). Depending on the initial conditions, the simulation time and the subsystem parameters, the mean value may get close to zero. Therefore, the variance is used in the denominator and not the mean value.

3.7.1 Implicit co-simulation method based on baumgarte stabilization

Fig. 21 in Appendix G (see Wiley online library) contains convergence plots for three different Baumgarte parameters, namely $\mu = 2.5E-4$, $\mu = 1E-3$ and $\mu = 5E-3$. The co-simulations were accomplished with a force/force-decomposition approach for $k = 0$, $k = 1$ and $k = 2$. The first row contains convergence plots for the index-1, the second row for the index-2 and the third row for the index-3 formulation.

For the index-1 approach we observe that the numerical error becomes larger, if μ is increased. However, stability is increased, if μ is increased. The convergence order is also influenced by the Baumgarte parameter. For $\mu = 5E-3$, we observe a convergence behavior according to $\mathcal{O}(H^1)$, $\mathcal{O}(H^2)$ and $\mathcal{O}(H^3)$ for the case of constant, linear and quadratic approximation polynomials. Decreasing μ, the convergence order is increased for $k = 0$ ($\mathcal{O}(H^1) \rightarrow \mathcal{O}(H^2)$).

In case of the index-2 formulation, only $k = 0$ yields stable results. The global error converges with $\mathcal{O}(H^2)$. The Baumgarte parameter μ has only little influence on the numerical error. Compared with the index-1 approach for $k = 0$, the index-2 formulation produces a smaller numerical error.

For the index-3 method, simulations for $k = 1$ and $k = 2$ are unstable. The numerical error is in the same range as in the index-2 case and converges with $\mathcal{O}(H^2)$. It should be mentioned that the straight dotted lines in the convergence plots are auxiliary lines, which indicate the convergence orders $\mathcal{O}(H^1)$, $\mathcal{O}(H^2)$, $\mathcal{O}(H^3)$, etc.

Remark: It should be stressed that the stability plots have been generated with the dimensionless Baumgarte parameters $\bar{\beta} = 2\bar{\mu}$ and $\bar{\gamma} = \bar{\mu}^2$, i.e. the Baumgarte parameters are scaled with the macro-step size H ($\bar{\beta} = \beta/H$, $\bar{\gamma} = \gamma/H^2$). The convergence plots have, however, been produced with non-dimensionless parameters $\beta = 2\mu$ and $\gamma = \mu^2$.

3.7.2 *Implicit co-simulation method based on weighted multiplier approach*

Convergence plots for the weighted multiplier approach are collected in Fig. 22 for three different parameter sets, namely $a = 0.5, b = 0.25$, $a = b = 1$ and $a = 2.5, b = 5$. The simulations were carried out with a force/force-decomposition approach for $k = 0, k = 1$ and $k = 2$. The first row contains convergence plots for the index-1 and the second row for the index-2 approach. It should be stressed again that the weighted multiplier and the Baumgarte approach have identical index-3 formulations.

In the index-1 case, we observe that for $k = 0$ the global error is only slightly affected by the weighted multiplier parameters a and b. Interesting are the index-1 plots for $a = b = 1$ and $a = 2.5$ and $b = 5$: the numerical error for $k = 1$ is significantly smaller than for the Baumgarte approach. Hence, with respect to stability and accuracy the index-1 method with $a = b = 1$ in combination with linear approximation polynomials shows a good performance. The index-1 plots also exhibit that the stability will be increased if the weighted multiplier parameters a and b are increased. For $k = 0$, the global error converges with $\mathcal{O}(H^2)$. For $k = 1$ and $k = 2$, a convergence behavior with $\mathcal{O}(H^4)$ is observed.

The results for the index-2 formulation are similar to the results obtained with the Baumgarte index-2 approach.

3.7.3 *Implicit co-simulation method based on projection technique*

In Fig. 23, a convergence plot is depicted for the projection method based on a force/force-coupling approach. Simulations have been carried out for $k = 0, k = 1$ and $k = 2$. We observe stable simulations for constant, linear and quadratic approximation. For $k = 0$, the magnitude of the global error is in the same range as for the weighted multiplier approach. For $k = 1$, the numerical error is larger compared with the index-1 weighted multiplier approach. For $k = 2$, the error is in the same range as for the index-1 weighted multiplier approach. The global error converges with $\mathcal{O}(H^2)$ for $k = 0$, with $\mathcal{O}(H^3)$ for $k = 1$ and with $\mathcal{O}(H^4)$ for $k = 2$.

4 Nonlinear example

In the previous sections, three co-simulation methods have been investigated with respect to their numerical stability and convergence behavior. For analyzing the numerical stability, Dahlquist's stability theory based on a linear test model has been applied and extended to co-simulation approaches. In order to show the applicability of the presented co-simulation approaches to nonlinear problems [34, 37], we consider the planar double pendulum depicted in Fig. 5. The pendulum consists of two rigid links. The system is decomposed into two subsystems and simulated by a co-simulation approach. The first link – representing subsystem 1 – is connected to ground by an atpoint joint (note that atpoint and revolute joint are equivalent in the planar case). The second link – representing subsystem 2 – is coupled to the first link by an atpoint joint. Gravity is acting in negative y-direction ($g = 9.81\,\mathrm{m/s^2}$). A linear viscous damping force is applied at the center of mass of both links (damping coefficients $d_x = d_y = 2\,\mathrm{Ns/m}$). The simulations were accomplished with the subsequent parameters: masses $m_1 = m_2 = 1\,\mathrm{kg}$, moments of inertia $J_1 = J_2 = 1/12\,\mathrm{kgm^2}$, lengths $l_1 = l_2 = 1\,\mathrm{m}$. As initial conditions, we chose $\varphi_{1,0} = \pi/4\,\mathrm{rad}$, $\varphi_{2,0} = -\pi/4\,\mathrm{rad}$, $\dot{\varphi}_{1,0} = \dot{\varphi}_{2,0} = 0\,\mathrm{rad/s}$. Both subsystems were integrated with an implicit Runge-Kutta method (relative and absolute error tolerance $\varepsilon_{rel} = \varepsilon_{abs} = 1E-6$).

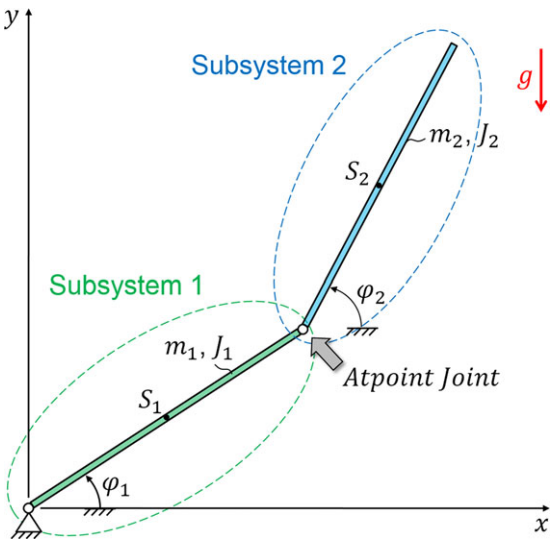

Fig. 5 Planar double pendulum: interpretation as two coupled subsystems.

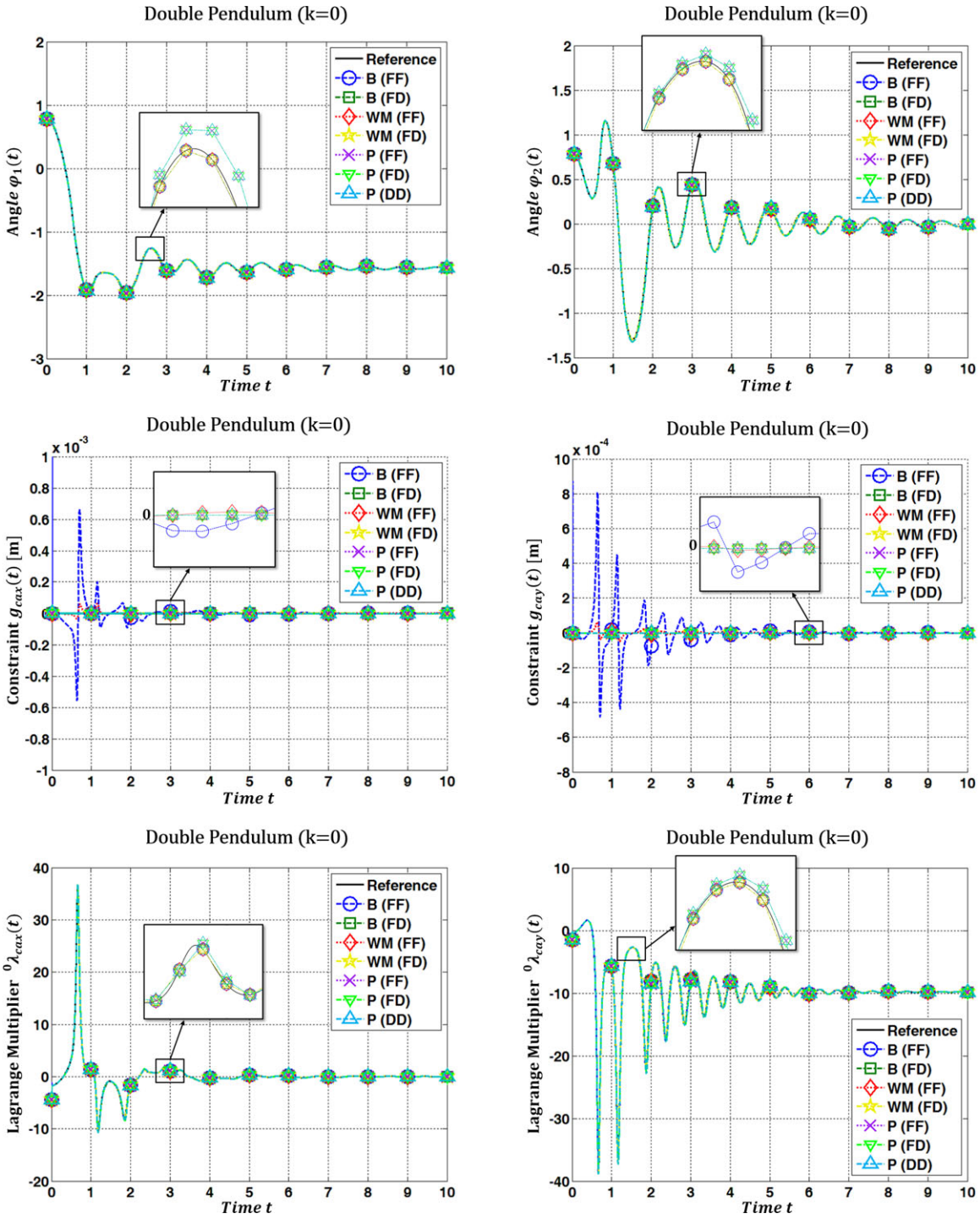

Fig. 6 Simulation results for the double pendulum for different coupling approaches and decomposition techniques for the case of constant approximation $(k = 0)$: angles $\varphi_1(t)$ and $\varphi_2(t)$, constraint equations $g_{cax}(t)$, $g_{cay}(t)$ and Lagrange multipliers $\lambda_{cax}(t)$, $\lambda_{cay}(t)$.

The nonlinear model is calculated with the three co-simulation approaches of Sect. 2 (Baumgarte, weighted multiplier and projection approach) using the three decomposition techniques (force/force-, force/displacement- and displacement/displacement-decomposition). In Fig. 6, simulation results are collected for the case of constant approximation polynomials $(k = 0)$. The figure shows the angles $\varphi_1(t)$ and $\varphi_2(t)$. Moreover, the constraint equations $g_{cax}(t) = (x_{S1} + l_1/2 \cdot \cos\varphi_1) - (x_{S2} - l_2/2 \cdot \cos\varphi_2)$ and $g_{cay}(t) = (y_{S1} + l_1/2 \cdot \sin\varphi_1) - (y_{S2} - l_2/2 \cdot \sin\varphi_2)$ for the atpoint joint connecting the two links are plotted. Note that x_{S1}, y_{S1} as well as x_{S2}, y_{S2} term the coordinates of the center of mass of the two links in horizontal and vertical direction. The figure also depicts the corresponding Lagrange multipliers (i.e. the reaction forces in horizontal

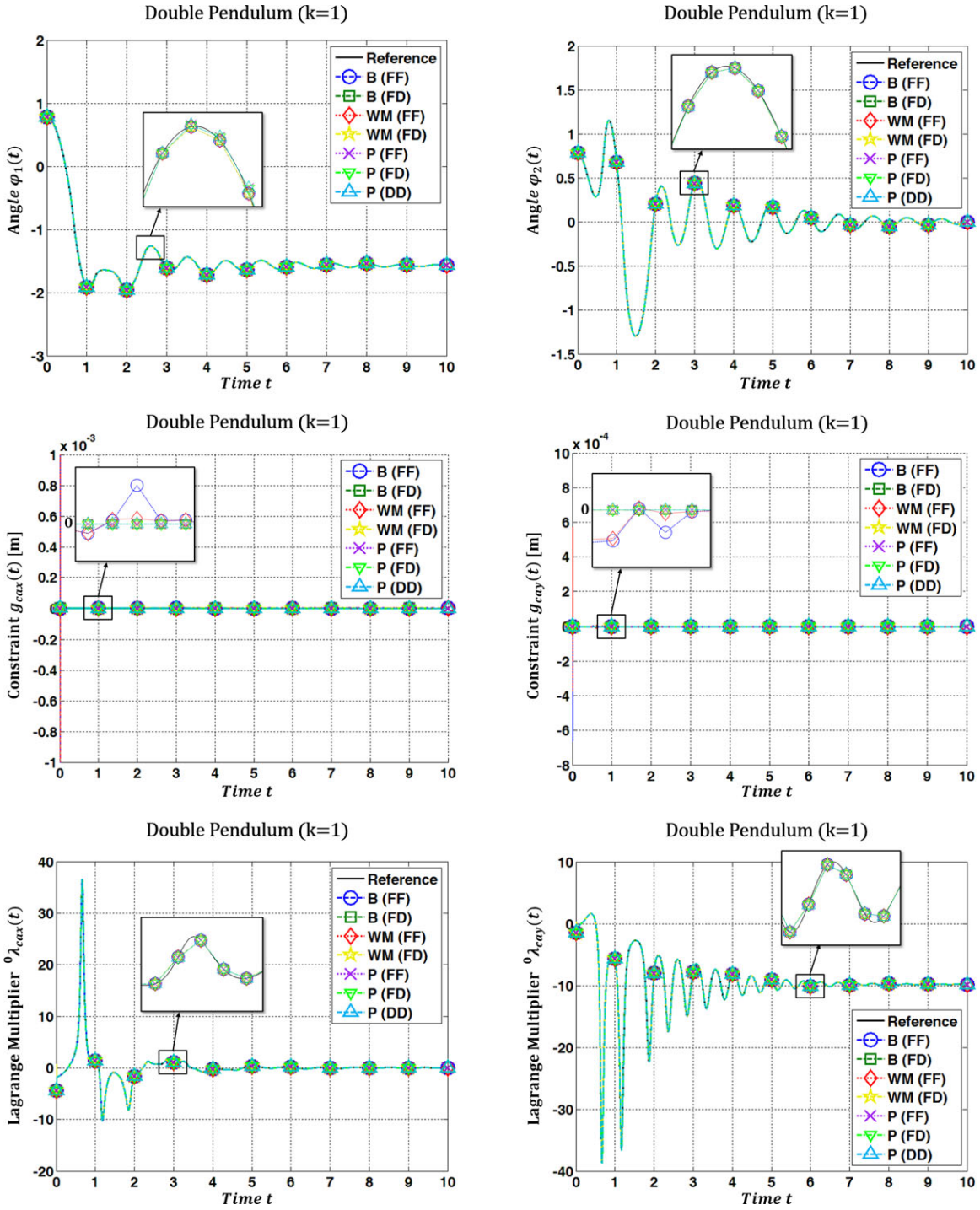

Fig. 7 Simulation results for the double pendulum for different coupling approaches and decomposition techniques for the case of linear approximation $(k = 1)$: angles $\varphi_1(t)$ and $\varphi_2(t)$, constraint equations $g_{cax}(t), g_{cay}(t)$ and Lagrange multipliers $\lambda_{cax}(t)$, $\lambda_{cay}(t)$.

and vertical direction) acting at the coupling joint. Corresponding simulation results for the case of linear and quadratic approximation polynomials are collected in Fig. 7 and Fig. 8. The simulations were carried out with the constant macro-step size $H = 1E - 3$. It should be mentioned that the reference solution was calculated numerically with a monolithic model.

All co-simulation approaches are stable with two exceptions: The weighted multiplier approach (force/force- and force/displacement-decomposition) is unstable for the case that quadratic approximation polynomials are used, see Fig. 8. This

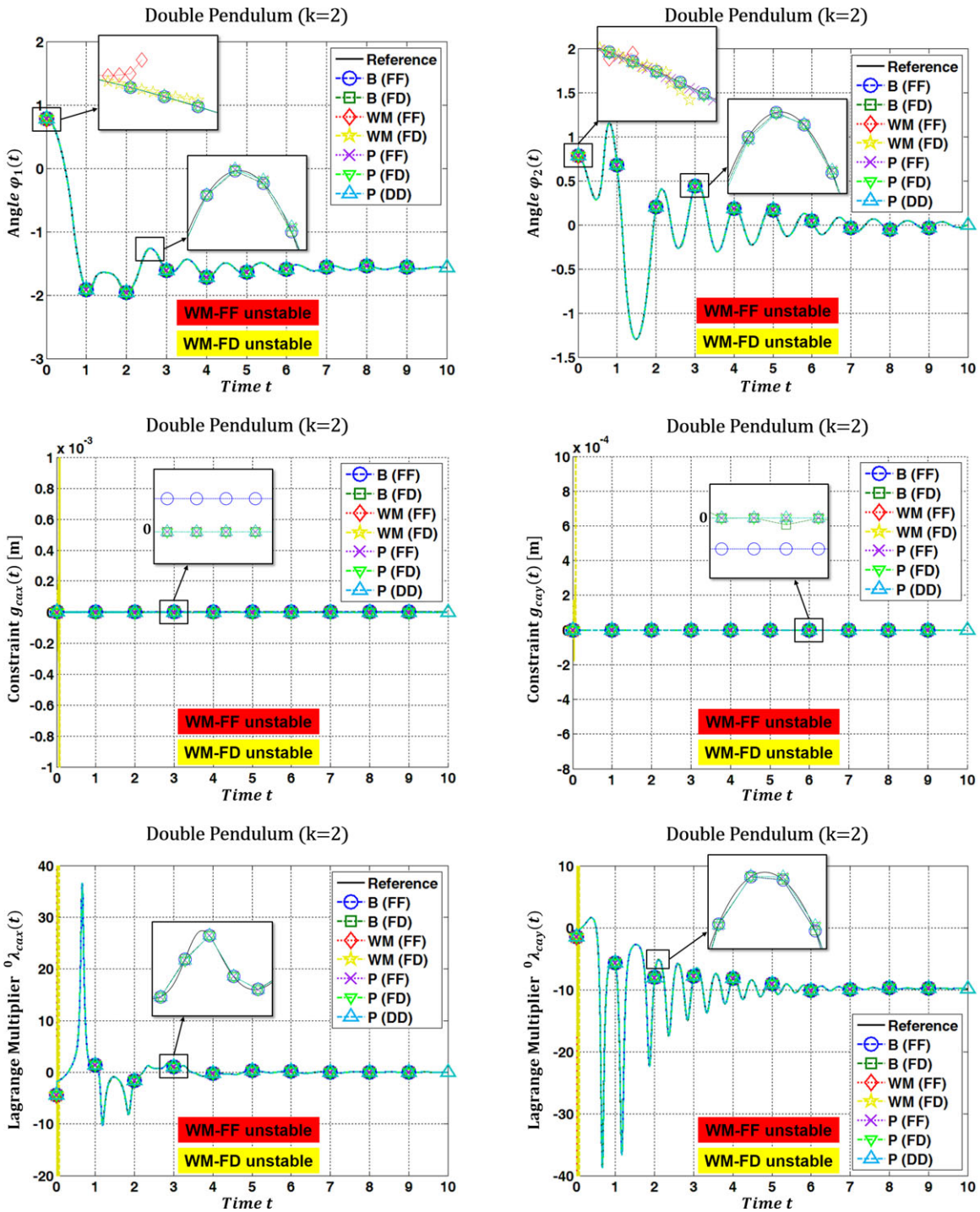

Fig. 8 Simulation results for the double pendulum for different coupling approaches and decomposition techniques for the case of quadratic approximation ($k = 2$): angles $\varphi_1(t)$ and $\varphi_2(t)$, constraint equations $g_{cax}(t)$, $g_{cay}(t)$ and Lagrange multipliers $\lambda_{cax}(t)$, $\lambda_{cay}(t)$.

correlates very well with the stability plots in Appendix A.2 and B.2 (right column) (see Wiley online library). Note, for instance, the zoom in the third plot in Fig. 10, which illustrates that for small damping ($\bar{\lambda}_{r1} \approx -0.1$), the co-simulation gets unstable. For the two-mass oscillator, $\bar{\lambda}_{r1} = -\bar{d}_1/2 = -(d_1 \cdot H)/(2m_1) < -0.1$ necessitates for $H = 1E-3$ and $m_1 = 1$ a damping parameter of $d_1 > 200$ for achieving stable results. The nonlinear model in Sect. 4 was integrated with a viscous damping parameter of 2 so that the instability of the nonlinear model may easily be explained with the help of the stability plots.

5 Conclusions

For analyzing the numerical stability of co-simulation methods, a test model has to be defined. The linear two-mass oscillator with one degree of freedom is the quite obvious choice. The stability of this co-simulation test model is characterized by 5 independent parameters ($\bar{\lambda}_{r1}$, $\bar{\lambda}_{i1}$, α_{m21}, $\alpha_{\lambda r21}$ and $\alpha_{\lambda i21}$). By discretizing the test model with a co-simulation method, one obtains a homogenous system of linear recurrence equations. The spectral radius of this recurrence system characterizes the stability of the underlying co-simulation method. To compare different co-simulation approaches, 2D stability plots are useful. Therefore, 3 of the 5 parameters are fixed so that the spectral radius can be plotted as a function of the remaining 2 parameters.

To illustrate the stability behavior of numerical time integration schemes, normally real and imaginary part of the eigenvalue in Dahlquist's test equation multiplied by the step-size h – i.e. $h\lambda_r$ and $h\lambda_i$ – are used as axes in 2D stability plots. According to that, the dimensionless real and imaginary part of the eigenvalue of subsystem 1 – i.e. $\bar{\lambda}_{r1}$ and $\bar{\lambda}_{i1}$ – are used as axes in 2D co-simulation stability plots. The remaining 3 parameters, namely the mass ratio coefficient α_{m21}, the damping ratio coefficient $\alpha_{\lambda r21}$ and the frequency ratio coefficient $\alpha_{\lambda i21}$ are held constant.

The results of the stability analysis for the Baumgarte and the weighted multiplier approach may be summarized as follows:

- For $k = 0$ (index-1 formulation), the Baumgarte approach with $\bar{\mu} = 1$ is more stable than the weighted multiplier approach with $a = b = 1$.
- For $k = 1$ (index-1 formulation), the Baumgarte approach with $\bar{\mu} = 1$ and the weighted multiplier approach with $a = b = 1$ show a similar stability behavior. Although the stability behavior of both methods is comparable, the numerical error of the weighted multiplier approach is notably smaller. Reducing $\bar{\mu}$ may decrease the numerical error, however with the drawback that the stability is reduced. Using linear approximation polynomials, the weighted multiplier approach with $a = b = 1$ seems to be a good choice.
- For $k = 2$ (index-1 formulation), stable results are obtained with the Baumgarte approach for $\bar{\mu} = 1$. The weighted multiplier method with $a = b = 1$, however, shows an unstable region close to the origin (loss of stability for $\bar{\lambda}_{r1}, \bar{\lambda}_{i1} \to 0$) and is therefore not suitable for practical applications.
- For $k = 0$ (index-1 formulation), stability of both methods may (slightly) be increased by reducing the parameters $\bar{\mu}$ and a, b, respectively.
- For $k = 1$ and $k = 2$ (index-1 formulation), stability of both methods can be increased by increasing the parameters $\bar{\mu}$ and a, b (with the drawback that the numerical error may be increased).
- Regarding the index-1 formulations, the force/displacement-decomposition approach shows for $k = 0$ a better stability behavior than the force/force-decomposition approach. For $k = 1$ and $k = 2$, however, force/force-decomposition reveals an improved stability behavior.
- The index-2 and the index-3 approaches (Baumgarte and weigthed mutliplier) exhibit a good stability behavior for $k = 0$.

The results of the stability analysis for the projection method can be summarized as follows:

- The displacement/displacement-decomposition approach exhibits a better stability behavior than the force/force- and the force/displacement-decomposition approach. For $k = 0$, the displacement/displacement-decomposition approach has shown only stable simulations in the considered parameter range.
- Using force/force- or displacement/displacement-decomposition, the stability behavior for constant approximation $(k = 0)$ is better than for linear $(k = 1)$ and quadratic $(k = 2)$ approximation.
- Stability is significantly influenced (reduced), if the subsystems have very different damping and frequency properties, i.e. if the damping ratio coefficient λ_{r21} and the frequency ratio coefficient λ_{i21} become larger.

A straightforward explanation of the stability behavior of the different co-simulation approaches is not possible. Although the test model is linear, the spectral radius ρ of the recurrence system is a highly nonlinear function of the five independent parameters of the co-simulation test model. In contrast to time integration methods, where the spectral radius may be calculated analytically as a function of $h\lambda_r$ and $h\lambda_i$, it is impossible to derive a closed analytical expression for $\rho(\bar{\lambda}_{r1}, \bar{\lambda}_{i1}, \alpha_{m21}, \alpha_{\lambda r21}, \alpha_{\lambda i21})$. The shape of some stability plots is quite regular, while other plots look rather irregular. The reason therefore cannot be explained easily. Complex shaped stability plots in connection with co-simulation and subcycling methods are reported in different works in literature, see e.g. [9–11, 31].

From the practical point of view, stability plots are important in order to compare different co-simulation methods and decomposition techniques. As has been shown, the stability behavior of the different coupling approaches differs considerably. Also, the approximation order has a significant influence on the numerical stability.

The plots also illustrate that it is not possible to find general rules and parameter dependencies for explicating the stability of the diverse approaches. For some methods, stability is decreased, if the approximation order is increased. It is, however, interesting to notice that for some approaches the usage of linear approximation polynomials yields more stable results than the application of constant approximation polynomials. Noticeable is also the fact that some plots exhibit an instable region close to the origin, i.e. the method gets unstable for $H \to 0$, which is especially important if a step-size controller is used for controlling the macro-step size.

Although some of the stability plots only reveal stable points in the considered parameter range for $\bar{\lambda}_{r1}$, $\bar{\lambda}_{i1}$ and thus seem to indicate A-stability and although other plots seem to indicate $A(\alpha)$-stability, neither A-stability nor $A(\alpha)$-stability can be proven, since the spectral radius can only be calculated numerically. Further simulations, which are not shown here, exhibit however that some of the co-simulation methods yield stable simulations also for very large values of $\bar{\lambda}_{r1}$ and $\bar{\lambda}_{i1}$ and in a wide range of the parameters α_{m21}, $\alpha_{\lambda r21}$ and $\alpha_{\lambda i21}$.

References

[1] J. Ambrosio, J. Pombo, F. Rauter, and M. Pereira, A Memory Based Communication in the Co-simulation of Multibody and Finite Element Codes for Pantograph-Catenary Interaction Simulation, in: C. L. Bottasso (ed.), Multibody Dynamics: Computational Methods and Applications (Springer, 2009) pp. 231–252.

[2] J. Ambrosio, J. Pombo, M. Pereira, P. Antunes, and A. Mosca, A computational procedure for the dynamic analysis of the catenary-pantograph interaction in high-speed trains, J. Theor. Appl. Mech. **50/3**, 681–699 (2012), Warsaw.

[3] J. Baumgarte, Stabilization of constraints and integrals of motion in dynamical systems, Comput. Methods Appl. Mech. Eng. **1**, 1–16 (1972).

[4] M. Busch and B. Schweizer, Numerical stability and accuracy of different co-simulation techniques: Analytical investigations based on a 2-DOF test model, in: Proceedings of The 1st Joint International Conference on Multibody System Dynamics, IMSD 2010, Lappeenranta, Finland, 25-27 May (2010).

[5] M. Busch and B. Schweizer, Coupled simulation of multibody and finite element systems: an efficient and robust semi-implicit coupling approach, Arch. Appl. Mech. **82**(6), 723–741 (2012).

[6] M. Busch and B. Schweizer, An explicit approach for controlling the macro-step size of co-simulation methods, in: Proceedings of The 7th European Nonlinear Dynamics, ENOC 2011, Rome, Italy, 24-29 July (2011).

[7] V. Carstens, R. Kemme, and S. Schmitt, Coupled simulation of flow-structure interaction in turbomachinery, Aerosp. Sci. Technol. **7**, 298–306 (2003).

[8] J. Cuadrado, J. Cardenal, P. Morer, and E. Bayo, Intelligent Simulation of Multibody Dynamics: Space-State and Descriptor Methods in Sequential and Parallel Computing Environments, Multibody Syst. Dyn. **4**, 55–73 (2000).

[9] W. J. T. Daniel, Analysis and implementation of a new constant acceleration subcycling algorithm, Int. J. Numer. Methods Eng. **40**, 2841–2855 (1997).

[10] W. J. T. Daniel, A study of the stability of subcycling algorithms in structural dynamics, Comput. Methods Appl. Mech. Engrg. **156**, 1–13 (1998).

[11] W. J. T. Daniel, A partial velocity approach to subcycling structural dynamics, Comput. Methods Appl. Mech. Engrg. **192**, 375–394 (2003).

[12] M. Datar, I. Stanciulescu, and D. Negrut, A Co-Simulation Framework for Full Vehicle Analysis, in: Proceedings of the SAE 2011 World Congress, SAE Technical Paper 2011-01-0516, 12-14 April, Detroit, Michigan, USA (2011).

[13] M. Datar, I. Stanciulescu, and D. Negrut, A co-simulation environment for high-fidelity virtual prototyping of vehicle systems, Int. J. Veh. Syst. Model. Test. **7**, 54–72 (2012).

[14] M. R. Dörfel and B. Simeon, Analysis and Acceleration of a Fluid-Structure Interaction Coupling Scheme, Numer. Math. Adv. Appl., pp. 307–315 (2010).

[15] P. Eberhard, T. Gaugele, U. Heisel, and M. Storchak, A Discrete Element Material Model Used in a Co-simulated Charpy Impact Test and for Heat Transfer, Proceedings 1st Int. Conference on Process Machine Interactions, Hannover, Germany, 3-4 September (2008).

[16] M. Friedrich and H. Ulbrich, A parallel co-simulation for mechatronic systems, in: Proceedings of The 1st Joint International Conference on Multibody System Dynamics, IMSD 2010, Lappeenranta, Finland, 25-27 May (2010).

[17] C. W. Gear and D. R. Wells, Multirate linear multistep methods, BIT **24**, 484–502 (1984).

[18] F. Gonzalez, M. Gonzalez, and J. Cuadrado, Weak coupling of multibody dynamics and block diagram simulation tools, in: Proceedings of the ASME 2009 International Design Engineering Technical Conferences & Computers and Information in Engineering Conference, IDETC/CIE 2009, San Diego, California, USA, August 30 - September 2 (2009).

[19] F. Gonzalez, M. A. Naya, A. Luaces, and M. Gonzalez, On the effect of multirate co-simulation techniques in the efficiency and accuracy of multibody system dynamics, Multibody Syst. Dyn. **2**(4), 461–483 (2011).

[20] B. Gu and H. H. Asada, Co-simulation of algebraically coupled dynamic subsystems without disclosure of proprietary subsystem models, J. Dyn. Syst. Meas. Control **126**, 1–13 (2004), DOI: 10.1115/1.1648307.

[21] E. Hairer, S. P. Norsett, and G. Wanner, Solving Ordinary Differential Equations I: Nonstiff Problems, 3rd ed. (Springer, 2009).

[22] E. Hairer and G. Wanner, Solving Ordinary Differential Equations II: Stiff and Differential-Algebraic Problems, 2nd ed. (Springer, 2010).
[23] S. Helduser, M. Stuewing, S. Liebig, and S. Dronka, Development of electro-hydraulic actuators using linked simulation and hardware-in-the-loop technology, in: C. Burrows, K. Edge (eds.), Power Transmission and Motion Control 2001, Bath, UK, pp. 49–56 (2001).
[24] G. Hippmann, M. Arnold, and M. Schittenhelm, Efficient simulation of bush and roller chain drives, in: J. Goicolea, J. Cuadrado, J. G. Orden (eds.), Proceedings of ECCOMAS Thematic Conference on Advances in Computational Multibody Dynamics, Madrid, pp. 1–18 (2005).
[25] R. Kübler and W. Schiehlen, Two methods of simulator coupling, Math. Comput. Model. Dyn. Syst. **6**, 93–113 (2000).
[26] A. Lehnart, F. Fleissner, and P. Eberhard, Using SPH in a Co-Simulation Approach to Simulate Sloshing in Tank Vehicles, Proceedings SPHERIC4, Nantes, France, 27–29 May (2009).
[27] Y. G. Liao and H. I. Du, Co-simulation of multi-body-based vehicle dynamics and an electric power steering control system, Proc. Inst. Mech. Eng. K, J. Multibody Dyn. **215**, 141–151 (2001).
[28] S. Meynen, J. Mayer, and M. Schäfer, Coupling Algorithms for the Numerical Simulation of Fluid-Structure-Interaction Problems, ECCOMAS 2000: European Congress on Computational Methods in Applied Sciences and Engineering, Barcelona (2000).
[29] M. Naya, J. Cuadrado, D. Dopico, and U. Lugris, An Efficient Unified Method for the Combined Simulation of Multibody and Hydraulic Dynamics: Comparison with Simplified and Co-Integration Approaches, Arch. Mech. Eng. **LVIII**, 223–243 (2011).
[30] N. Negrut, D. Melanz, H. Mazhar, D. Lamb, and P. Jayakumar, Investigating Through Simulation the Mobility of Light Tracked Vehicles Operating on Discrete Granular Terrain, SAE Int, JPasseng. Cars - Mech. Syst. **6**, 369–381, DOI: 10.4271/2013-01-1191, 2013.
[31] V. Savcenco, Comparison of the asymptotic stability properties for two multirate strategies, J. Comput. Appl. Math. **220**, 508–524 (2008).
[32] M. Schäfer, S. Yigit, and M. Heck, Implicit Partitioned Fluid-Structure Interaction Coupling, ASME, PVP2006-ICPVT11-93184, Vancouver, Canada (2006).
[33] R. Schmoll and B. Schweizer, Co-simulation of multibody and hydraulic systems: comparison of different coupling approaches, Multibody Dynamics 2011, ECCOMAS Thematic Conference, J. C. Samin, P. Fisette (eds.), Brussels, Belgium, 4–7 July (2011), pp. 1-13.
[34] B. Schweizer and D. Lu, Predictor/Corrector co-simulation approaches for solver coupling with algebraic constraints, ZAMM - J. Appl. Math. Mech. **95**, 911–938 (2015).
[35] B. Schweizer and D. Lu, Co-Simulation Methods for Solver Coupling with Algebraic Constraints: Semi-Implicit Coupling Techniques, in: Proceedings of The 3rd Joint International Conference on Multibody System Dynamics and The 7th Asian Conference on Multibody Dynamics, IMSD 2014, ACMD 2014, Bexco, Busan, Korea, June 30-July 3 (2014).
[36] B. Schweizer and D. Lu, Semi-Implicit Co-Simulation Approach for Solver Coupling, Arch. Appl. Mech., DOI: 10.1007/s00419-014-0883-5 (2014).
[37] B. Schweizer and D. Lu, Stabilized index-2 co-simulation approach for solver coupling with algebraic constraints, Multibody Syst. Dyn., DOI: 10.1007/s11044-014-9422-y (2014).
[38] B. Schweizer, P. Li and D. Lu, Explicit and implicit co-simulation methods: stability and convergence analysis for different solver coupling approaches, J. Comput. Nonlinear Dyn., doi:10.1115/1.4028503 (2014).
[39] B. Schweizer, P. Li, D. Lu, and T. Meyer, Stabilized Implicit Co-Simulation Methods: Solver Coupling Based on Constitutive Laws, Arch. Appl. Mech., doi:10.1007/s00419-015-0999-2 (2015).
[40] B. Schweizer, P. Li, D. Lu, and T. Meyer, Stabilized implicit co-simulation method: solver coupling with algebraic constraints for multibody systems, J. Comput. Nonlinear Dyn., doi:10.1115/1.4030508 (2015).
[41] B. Schweizer, D. Lu, P. Li, Co-simulation method for solver coupling with algebraic constraints incorporating relaxation techniques, Multibody Syst. Dyn., DOI: 10.1007/s11044-015-9464-9 (2015).
[42] F. Spreng, P. Eberhard, and F. Fleissner, An approach for the coupled simulation of machining processes using multibody system and smoothed particle hydrodynamics algorithms, Theor. Appl. Mech. Lett. **3**(1), 8–013005 (2013).
[43] A. Verhoeven, B. Tasic, T. G. J. Beelen, E. J. W. ter Maten, and R. M. M. Mattheij, BDF Compound-Fast Multirate Transient Analysis with Adaptive Stepsize Control, J. Numer. Anal. Ind. Appl. Math. **3**(3–4), 275–297 (2008).
[44] S. Wuensche, C. Clauß, P. Schwarz, and F. Winkler, Electro-thermal circuit simulation using simulator coupling, IEEE Trans. Very Large Scale Integ. (VLSI) Syst. **5**, 277–282 (1997).

